PERFORMANCE EVALUATION OF CONTROL STRATEGIES FOR GRID CONNECTED WIND POWER GENERATOR

By

WELCOME KHULEKANI NTULI

Student No: 21225735

Dissertation submitted in fulfillment of the requirements for the degree of Master of Engineering in the Department of Electrical Power Engineering, Faculty of Engineering and the Built Environment

Durban University of Technology
South Africa

Supervisor: Dr Musasa Kabeya
Co-Supervisor: Dr Gulshan Sharma

July 2022

I CONCUR TO THE SUBMISSION OF THIS DISSERTATION AS THE CANDIDATE'S SUPERVISOR.

Dr Musasa Kabeya _____ ____ _____

NAME OF SUPERVISOR SIGNATURE

Dr Gulshan Sharma _____ ___ ___

NAME OF CO-SUPERVISOR SIGNATURE

DECLARATION

By signing this document, I vouch for the originality of this dissertation and the accurate citation of all sources. Furthermore, this work has never been published in part or whole at any other institution.

This research was duly supervised by Dr M Kabeya and Dr G Sharma at the Durban University of Technology.

Submitted by:

..... 2022/10/25

Mr Welcome Khulekani Ntuli Date

DEDICATION

This research is dedicated to the memory of my late father, Mr Fano Ntuli, and mother, Mrs Goodness Nkosingiphile Ntuli.

ACKNOWLEDGMENT

- I would like to express my gratitude to Dr Musasa Kabeya, my supervisor, for being patient with me and offering excellent support in a highly professional manner.
- I would like to convey my appreciation to Dr G Sharma, my co-supervisor, for his exceptional support and guidance, as well as for providing me with the opportunity to conduct tutorial sections with undergraduate students. I am immensely appreciative of your expert instruction and supervision.
- I would want to express my gratitude to my family members for their assistance throughout the program (Xolani Ntuli, Lindiwe Ntuli, Mlungisi Ntuli). Finally, Kwanele Ntuli, my first-born, may God bless you in your studies.
- I would like to thank NRF for giving me mental and financial support during my studies (Ref No. MND200608529116).

ABSTRACT

South Africa is currently experiencing a significant load-shedding situation because of rising electricity demand. The renewable energy power producer (RPP) sector is growing rapidly to become an important source of power in South Africa and nations across the globe. Companies within this sector provide a variety of clean energy sources, including wind, solar, hydroelectric, biomass and geothermal. Despite its ability to support the power system and conserve the environment that sustains life, the rising usage of renewable distributed generators (RDGs) poses power quality problems in the overall distribution network, such as the voltage instability at buses, the increase in voltage/current harmonics distortions, etc. The technical requirements for connecting RDGs to the power system have been defined in standard grid code to ensure the safe, secure and proper functioning of the overall power system. The specifications defined in the grid code include the limit of voltage variations (i.e., +/-1 pu), the limit of frequency variations (i.e., +/-5%), and the limit of current/voltage harmonic distortions (i.e., total harmonic distortion voltage (THDv) of 0.1% and total harmonic distortion current (THDi) of 5%), and a power factor limit of Pf = (0.9-0.95). Additionally, RDGs must remain connected throughout a fault condition and assist in voltage recovery.

In this dissertation, control strategies for grid connected wind energy conversion system (WECS) are investigated for dynamic performance evaluation. This work focuses on the doubly fed induction generator (DFIG) – based WECS incorporating a proportional integral (PI) controller; the permanent magnet synchronous generator (PMSG) – based WECS incorporating a PI controller; DFIGb-based WECS incorporating a voltage source converter (VSC) with a fuzzy-logic controller, the proportional integral derivative (PID), and fuzzy-PID controller. A comparative analysis of the different WECS topologies was further conducted in terms of the steady-state error, the percentage overshoot, and the settling time of the voltage/current or power output signals and dc-link voltage signals.The VSC was selected as compared to the line-commutated converters (LCCs) because of the commutation that is not dependent on voltage and current AC signals. The grid-side converter was applied to regulate DC-link voltage and reactive power to their reference values. The rotor side converter provided rotor speed regulation on the DFIG to control

the power output signal. The vector control method was used for the dynamic performance analysis. The simulations were done using MATLAB/SIMULINK. From the simulation results, it was found that the DFIG-based WECS incorporating a fuzzy-PID controller performed efficiently compared to the other topologies of WECS.

TABLE OF CONTENTS

LIST OF FIGURES

LIST OF TABLES

LIST OF ACRONYMS AND SYMBOLS

REPP	Renewable Energy Power Producer
RDGs	Renewable Distributed Generators
THDv	Total Harmonic Distortion Voltage
THDc	Total Harmonic Distortion Current
WECS	Wind Energy Conversion System
DFIG	Doubly Fed Induction Generator
PMSG	Permanent Magnet Synchronous Generator
VSC	Voltage Source Converter
PID	Proportional Integral Derivative
LCCS	Line Commutated Converters
AC	Alternating Current
DC	Direct Current
THDs	Total Harmonic Distortions
MW	Mega Watts
IPP	Independent Power Producers
Tx	Transmission Network
Dx	Distribution Network
POC	Point of Connection
NSP	Network Service Provider
KV	Kilo Volts
NIPS	National Integrated Power System
P	Active Power

Q	Reactive Power
f	Frequency
HAWT	Horizontal Axis Wind Turbine
VAWT	Vertical Axis Wind Turbine
Te	Electromagnetic Torque
ωr	Rotor Speed
Tm	Mechanical Torque
Ids	direct axis stator current
Iqs	quadrature axis stator current
Vdr	rotor direct axis voltage
Vqr	rotor quadrature axis voltage
Rs	stator resistance
Pm	Mechanical Power
Rr	rotor resistance
Cp	Power coefficient
Pref	reference active power
GSC	Grid Side Converter
RSC	Rotor Side Converter
PWM	Pulse Width Modulation
NV	Negative Very large
PV	Positive Very large
NL	Negative Large
NB	Negative Big
NM	Negative Medium

NS	Negative Small
ZR	Zero
PS	Positive Small
PM	Positive Medium
PB	Positive Big
PL	Positive Large

CHAPTER 1:

INTRODUCTION

1.1. Background and motivation

South Africa's population expansion has placed Eskom just on the edge of losing its potential to provide energy to the nation adequately. This has prompted Eskom to implement load-shedding to stabilize the electricity grid. However, load-shedding is not a suitable approach for economic development and attracting foreign investors. Electricity generation/power system stability is the major factor driving economic security in both developing and industrialized nations. However, the nation is not only suffering from a load demand dilemma, as the current approach to power generation also contributes significantly to environmental pollution and global warming. Consequently, the most significant contributor to the emission of greenhouse gases is the predominant mode of energy production (i.e. Thermal power stations) [1].

South Africa and other countries across the world have adopted the integrated resource plan's policy. South Africa established this plan in 2011 and amended it over several years (2016, 2018 and 2019). In addition, the development of an integrated generator system is anticipated to fulfil the increasing load demand by 2030. To meet load demand, the renewable energy power producer (REPP) industry is expanding rapidly to merge with the current generation method. This industry provides a variety of renewable energy sources, such as wind, solar, hydroelectric, biomass and geothermal [2]. Renewable distributed generators (RDGs) are expected to account for approximately 42% of total power capacity by 2030 [3].

1.2. Problem statement

Wind power generators are the most environmentally friendly way to generate energy in the long run. However, the primary energy source (wind energy) used to generate electricity is not stable. As a result, when the wind power generator is connected to the power system, it has an impact on the dynamic performance of the power system, such as frequency stability, transient stability, voltage stability, power oscillation (active and reactive power), and . increases in voltage/current total harmonic distortion (THD) [4].

Different researchers and industries have used proportional integral (PI) controllers to compensate for active and reactive power. This control strategy, however, is insufficient for nonlinear systems such as wind power generators. Below is a list of some of the technical challenges of integrating wind farms into the power system:

1.2.1. Unsteady Frequency:

In an inter-connected system, the variation of frequency is highly affected by the rate of change of active power. However, this problem is usually mitigated via an optimal control method of active power or power balancing between supply and demand.

1.2.2. Voltage dips:

This is a temporary decrease in the normal rms voltage value over a short period of time. The percentage of acceptable voltage dip in South Africa is about 90% of the nominal rms voltage as per the IE61000-4-30 Standard. Voltage dips in a power system are caused by the change of load and reduction of nominal voltage. Hence, this problem may be mitigated via optimal control strategies of reactive power.

1.2.3. Harmonics:

Harmonics are unwanted disturbances occurring in a power system, caused by non-linear loads. These may develop in both the sending end and receiving end of the power system. Harmonics has greater input into line losses, which can cause overheating and the early ageing of machinery. Allowable voltage/current total harmonic distortion is between 5% and 3% depending on the system power rating as per IEEE519-1992. In South Africa, the power system is designed to operate at a frequency of 50 HZ. However, certain loads produce a frequency that are much greater than the rated frequency, such as power electronic converters that are more often utilised in renewable energy conversion systems. Hence, harmonics generate pollution in a sinusoidal ac waveform.

1.3. Aims and objectives

A. The main objective of this study is to investigate the dynamic performance of a DFIG-based WECS incorporating a voltage source converter (VSC) with a fuzzy-PID controller connected to a grid.
B. Support the power system during fault conditions by injecting or absorbing reactive power.
C. Control the amount of active power injected or absorbed based on the state of the power system to provide frequency stability.
D. Controlling reactive power as close to zero as possible during normal operating conditions or when the grid fault is cleared.

Additionally, a comparison of the suggested topology with the present one is performed, which includes:

- The DFIG-based WECS with a PID controller connected to a grid;
- The PMSG-based WECS with a PID controller connected to a grid; and
- The DFIG-based WECS with a Fuzzy logic controller.

The comparison of performance is drawn in terms of the percentage overshoot and undershoot, the settling time of the voltage and current signals, and in terms of the fault ride through capability.

1.4. Research questions

- What topology of WECS and control method can be used in wind farms in order to meet the South African grid code requirements when the wind farm is connected to grid?
- What is the impact of a wind farm connected to the power system infrastructure?
- What is the WECS protection method against grid faults?
- What is the effect of disconnecting and reconnecting wind farms while in operation due to cut-in and cut-off wind speeds?

1.5. Research contributions

This research will aid in identifying a suitable topology of WECS, including the control strategies, for renewable distributed generators (RDGs) and renewable integration

application. In addition, this study will assist the REPP sector in the development of RDGs that meet grid-code criteria. The increase of RDGs integrated into the power network will therefore alleviate the load demand situation.

1.6. Hypothesis

- The hybrid control techniques of fuzzy-logic controller and proportional integral derivative (PID) will provide robust control of wind power generator output signals (active and reactive power control). As a result, the fault ride through capabilities will be met in accordance with standard grid codes.

1.7. Arrangement of Thesis

- The **first chapter** provides the motivation for the research, problem statement, aims and objectives, and main contributions of the research.
- The technology of wind farms and standard grid codes when connecting wind farms to grid is provided in **Chapter 2**.
- **Chapter 3** reviews the different methods of control for WECS.
- **Chapter 4** entails modelling of the DFIG-based wind-energy conversion system with a VSC-PMW and fuzzy-PID controller connected to a grid.
- **Chapter 5** presents the results analysis and discussion.
- **Chapter 6** draws the conclusion and scope for future research.

1.8. List of publications

- W.K. Ntuli, G. Sharma, and M. Kabeya. Study of Fault Ride-Through Capability of Doubly Fed Induction Generator Based Wind Turbine. In 2022 30th South African Universities Power Engineering Conference (SAUPEC2022), South Africa, Durban.
- W.K. Ntuli, G. Sharma, and M. Kabeya. A Comparative Study of DFIG-based Wind Energy Conversion Systems with Fuzzy-PID and Fuzzy Logic Controller. In 2022 IEEE PES/IAS Power Africa Conference, Rwanda, Kigali.

- W.K. Ntuli, G. Sharma, and M. Kabeya. Development of Grid-Connected Renewable Generation Control Techniques. In 2022 IEEE PES/IAS PowerAfrica Conference, Rwanda, Kigali.
- W.K. Ntuli, M. Kabeya, G. Sharma. A comparative study of wind-energy conversion systems incorporating the DFIG and the PMSG. 2022 International Conference on Intelligent and Innovative Computing Applications (ICONIC), ISBN of Conference Proceedings: 978-99949-0-888-2.

CHAPTER 2:

REVIEW OF RENEWABLE ENERGY TECHNOLOGY AND STANDARD GRID CODES

2.1. Introduction

This chapter discusses the various renewable power generating technologies available in South Africa, as well as the grid codes that apply when connecting renewable distributed generators to power system.

2.2. South Africa's Power Generation Technologies and Capacity (MW)

South Africa's electricity industry is experiencing exponential growth, quality innovations, and significant structural changes. It has become a global trend to provide enough energy to meet rising energy demand while also lowering end-user bills by allowing competition to enter the electricity industry. As a result, power generation must meet end-user demand to boost the country's economy. The structure of South Africa's electrical power industry is depicted in Figure 2.1. This structure clearly indicates Eskom's contributions to the power grid, as well as the contributions of the Independent Power Producers (IPPs) sector and municipalities to the power grid. According to recent research, approximately 95% of Eskom's transmission generation comes from thermal stations (coal-fired power plants) and 60% goes to distribution, with municipalities responsible for the remaining 40% on the distribution network. Due to the exponential growth of the human population, Eskom's generation capacity cannot keep up with population growth. As a result, severe load shedding occurs, which may result in the economy failing as electricity is the primary energy source for South Africa's economy [5].

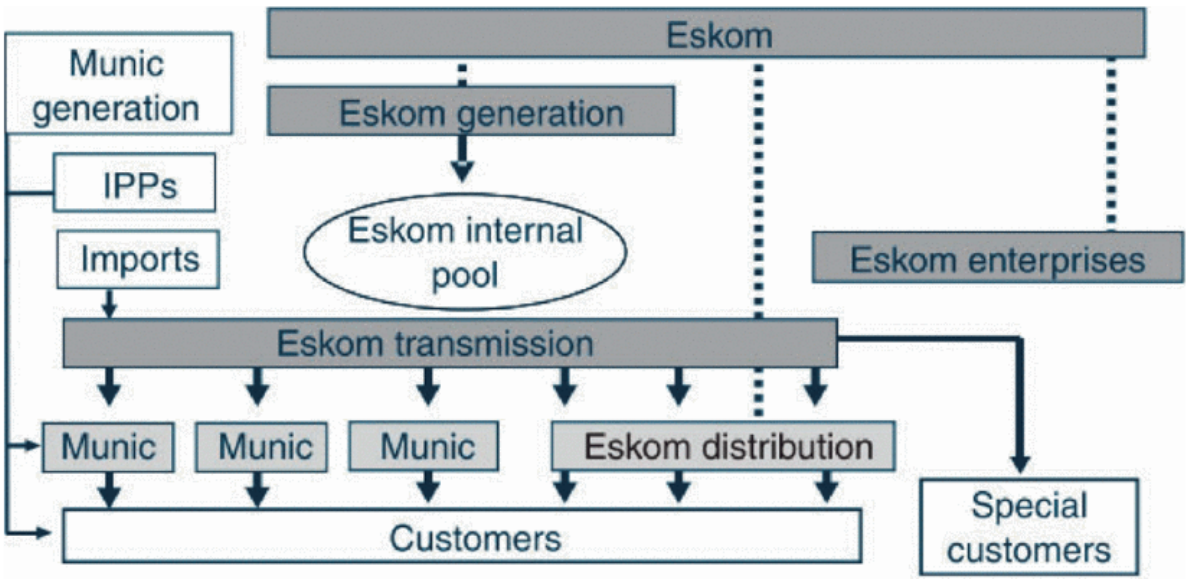

Figure 2.1 South Africa's Electrical Power Industry Structure [5].

South Africa has an annual capacity of approximately 229 200 gigawatt-hours of electricity. Approximately 12 000 gigawatts of electricity are supplied to Southern African countries (SADC) [5]. South Africa also imports approximately 9000Gwh per year from a hydroelectric power plant in Mozambique called Cahora Bassa. This is achieved by installing a 1.920-Megawatt direct current high voltage transmission network and importing roughly 1500 Megawatts to South Africa. Table 2.1 details the energy generation technologies available in South Africa, along with their output capacity (MW):

Table 2.1 Energy generation technologies in South Africa [5].

Energy generation technologies	**Size in Megawatts (MW)**
Coal	40.036
Gas	3.449
Hydro-electric	3.573
Wind-power	2.096
Nuclear plant	1.860
Photovoltaic solar	1.479
Concentrated solar power	40.0
Landfill Gas	7.5
Imported Hydro	1500

2.3. Standard Grid Code - South Africa

Historically, RDGs were permitted to disengage from the power system in the event of power system disturbances to avoid major devastation. In this modern era, RDGs are required to remain connected to the grid in the present or in the event of a fault [6]. To maintain the system stability and quality of supply, The standard grid code specifies the operating conditions for RDGs that are linked to a power system. South African standard codes state that, RDGs are expected to supply reactive power to boost grid voltage recovery during faults, and when grid fault clears, RDGs must continue to deliver active power into the grid [7]. It is more essential to consider these requirements when designing a control model of the wind energy system. Hence, these requirements improve power system performance during system disturbances and normal operating conditions. RDGs refers to a variety of technologies that generate electricity at or near where it will be used, such as photovoltaic systems, concentrated solar powers, small hydro power plants, landfill gas, biomass, biogas, wind systems, etc.

In the case of a major replacement or modification to a grid connected RDG, the RDG must report/undergo grid requirements procedures to ensure that it is still eligible to connect to power system. RDGs are classified into three groups according to their ratings at point of connection (POC). These RDGs are categorized as shown in the following Table 2.2:

Table 2.2 Groups of RDGs [8].

RDG Group	RDGs Ratings
Group A1	0 to 0.0138 MVA
Group A2	0.0138 MVA to 0.1 MVA
Group A3	0.1 MVA to1 MVA
Group B	1 MVA to 20 MVA
Group C	20 MVA and more

2.3.1. Tolerances for frequency and voltage variations are defined as follows:

According to this grid connection code, the RDGs must withstand frequency and voltage changes at the POC in both normal and unusual operation scenarios while using the least amount of active power. According to the specification of this grid

connection regulation, RDGs must be capable of providing voltage and frequency support.

Group A RDGs should be built to run continuously at a voltage between -15 and +10% of the POC's normal voltage. The actual operating voltage varies by location, which is chosen by the NSP in collaboration with the affected consumer and executed by the RDG. Group B and C RDGs must be designed to operate continuously within the POC voltage range given by U_{min} and U_{max}, as shown in Table 2.3, as measured at the POC.

Table 2.3 Minimum and maximum nominal operating voltages for RDGs in Group A& B [8].

Nominal Voltage in KV	**Per-unit Minimum Voltage**	**Per-unit Maximum Voltage**
132	0.90	1.0985
88	0.90	1.0985
66	0.9	1.0985
44	0.90	1.08
33	0.90	1.08
22	0.90	1.08
11	0.90	1.08

The National Integrated Power System (NIPS) has a nominal frequency of 50 Hz and is generally controlled within the parameters set out in the grid code. Figure 2.2 depicts the minimal operating ranges for the RDG (total cumulative over the life of the RDG) and Figure 2.3 (during a system frequency disturbance). When the NIPS frequency exceeds 51.5 Hz for more than 4 seconds, the RDG must be unplugged from the grid. The RDG may be unplugged if the frequency on the NIPS is less than 47.0 Hz for more than 200 ms. The RDG must stay connected to the NIPS throughout the rate of change of frequency values up to and including 1.5 Hz, if the network

frequency remains within the minimum operational range shown in Figures 2.2 and 2.3, respectively.

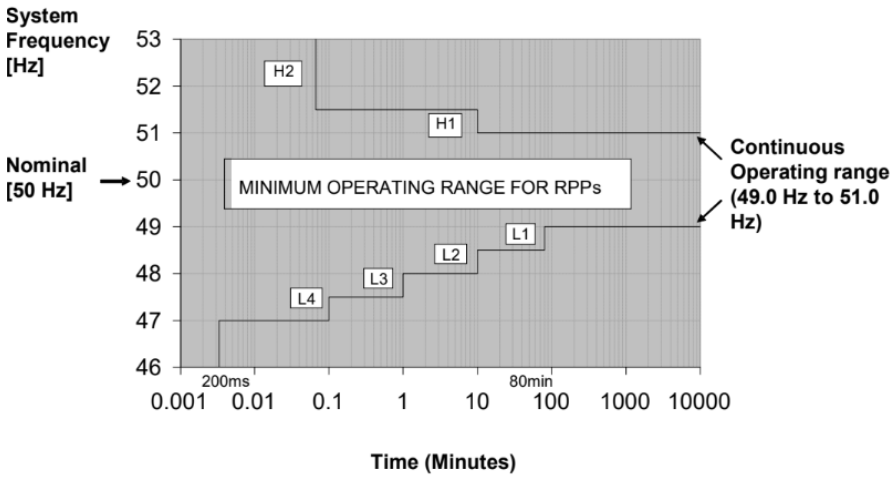

Figure 2.2 Minimum frequency operating range for RDGs [8].

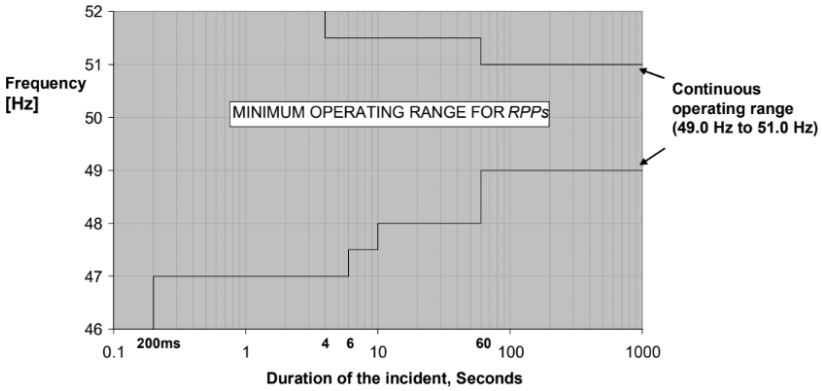

Figure 2.3 Frequency Disturbances [8].

Connecting to the National Integrated Power System (NIPS). Group A RDGs will be allowed to connect to the NIPS for no more than 60 seconds after:

- The voltage at the point of interconnection ranges from -15 to +10% of the typical voltage.
- The NIPS operates at a frequency between 49.0 Hz and 50.2 Hz, or as otherwise negotiated with the SO.

Group B and C RDGs shall be permitted to connect to the NIPS no later than three seconds after:

- The voltage at the POC is within 5% of the normal voltage for Tx-connected RDGs.

- For Dx-connected RDGs, the voltage at the POC is between U_{max} and U_{min}, as defined in Table 2.3, and is close to the nominal voltage.
- The NIPS operates at a frequency between 49.0 Hz and 50.2 Hz, or as otherwise negotiated with the SO.

2.3.2. RDGs and Voltage Ride-Through Capability

The RDG must be able to endure rapid phase jumps of up to 20 degrees at the POC without disconnecting or lowering output. After a period, the RDG must start regular production no later than 5 seconds after the operating conditions in the POC have returned to normal operating circumstances. RDGs in Group A must be built to withstand and fulfil the voltage ride through the circumstances depicted in Figure 2.4 below at the POC:

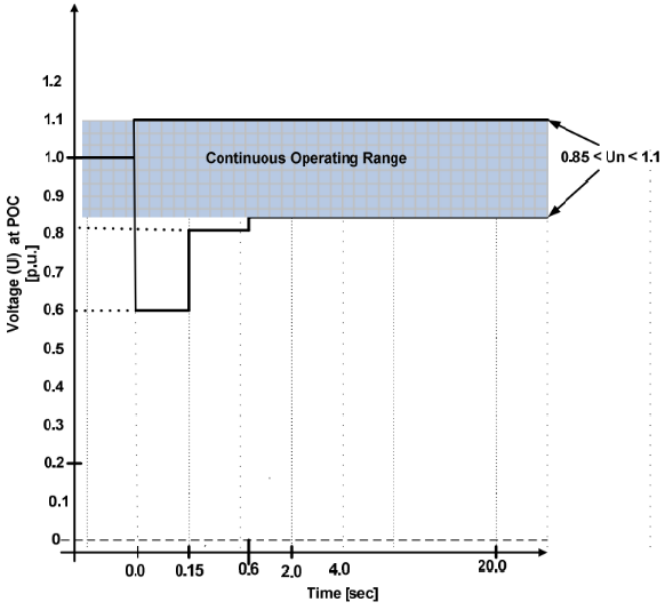

Figure 2.4 Voltage ride through capability for the RDG of Group A [8]. .

Furthermore, the maximum disconnection times for RDGs in Group A are shown in Table 2.4 below:

Table 2.4 Voltage deviation and time for tripping [8].

Percentage Voltage deviation	**Tripping duration**
Voltage greater than 50%	0.2s

Voltage greater than 50% or less than 85%	2s
Voltage greater than 85% or less than 110%	Normal operating zone
Voltage greater than 110% or less than 120%	2s
Voltage less than 120%	0.16s

a. Group B and C for RDGs

RDGs of Group B and C must be designed to withstand and fulfil the voltage requirements indicated in this section and depicted in Figure 2.5 and Figure 2.6, respectively [9]. Area D is exclusively relevant to RDGs in Group C. As demonstrated in Figure 2.5, the RDG must be designed to withstand voltage drops and surges, as well as supply or absorb reactive current as shown in Figure 2.6, without disconnecting. The RDG must be able to tolerate voltage decreases to zero as measured at the POC for a minimum of 0.150 seconds without disconnecting, as seen in Figure 2.5. As shown in Figure 2.5 the RDG in Group C should be able to withstand voltage increases of up to 120 percent of the rated voltage as measured at the POC for at least two seconds. Figure 2.5 works for both symmetrical and asymmetrical faults and the bold line shows the minimum voltage of all phases.

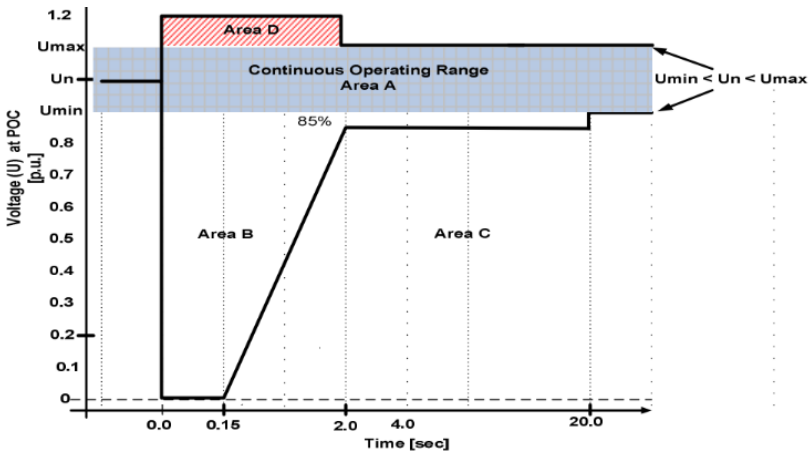

Figure 2.5 Voltage ride through capability for the RDG of Group B&C [10]. .

If the voltage returns to region A during the fault sequence, any additional voltage dips are considered a new fault condition. Disconnection is permitted if multiple subsequent fault sequences occur within region B and grow into area C, as shown in Figure 2.5 [10]. In combination with symmetrical fault sequences in areas B and D of Figure 2.5, the RDG (other than synchronous generator units) must be capable of managing reactive current, as shown in Figure 2.6. The prerequisites listed below must be met:

- **Area A:** The RDG must remain linked to the network and maintain normal production.
- **Area B:** The RDG must remain connected to the network and, in addition, RDGs of Group B and C must provide maximum voltage support by supplying a controlled amount of reactive current to help with voltage stabilisation, as seen in Figure 2.6.
- **Area D:** The RDG must remain connected to the network and provide maximum voltage support by absorbing a controlled amount of reactive current, ensuring that the RDG contributes to voltage stabilization within the RDG's design capabilities, as seen in Figure 2.6.
- **Area E** (in Figure 2.6): When the voltage at the POC falls below 20%, the RDG must continue to produce reactive current within its technical design restrictions to guarantee that the RDG contributes to voltage stabilization. Disconnection is only permitted if the conditions in Figure 2.6 are met.

Figure 2.6 shows how to manage the reactive current so that it follows the control characteristic with a tolerance of +/-20% after 60 seconds. In region B, the supply of reactive power takes precedence over the supply of active power. Active power must be maintained during voltage reductions, although for voltage drops of less than 85 percent, a reduction in active power within the RDG's design requirements is necessary. Within 1 second of the fault being cleared, each RDG must restore active power generation to at least 90% of the level available immediately prior to the problem.

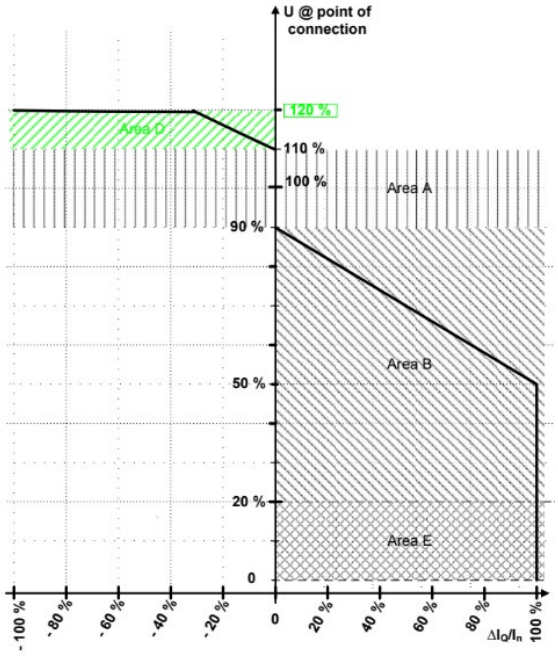

Figure 2.6 Grid code requirement of reactive power support [11].

2.3.3. RDGs of Group C - power frequency response

RDGs should be built to give power-frequency responses, as shown in Figure 2.7. Except for the necessary high frequency response (above 50.5 Hz), the RDG shall not execute any frequency response functions (i.e., no P_{delta} dead-band and control-band functions shall be implemented) unless a formal agreement with the SO has been entered. It must be possible to configure the frequency response control function for all the frequency points depicted in Figure 2.7. It must be possible to set the frequencies F_{min}, F_{max}, and F1 to F6 to any value between 47 and 52 Hz with a minimum accuracy of 10 mHz. The frequency points F1 to F4 are used to create a dead band and a control band for RPPs contracted for primary frequency responses. The objective of frequency points F_4–F_6 is to provide the required critical power/frequency response. Figure 2.7 shows the frequency control droop settings that must be implemented in the RDG. Each drooping option must be adjustable between 0% and 10%. The actual droop setting must be agreed upon with the SO. Individual RDG units may be shut off if the active power from the RDG is regulated downward below the unit's design limit, P_{min}. The RDGs (except for the RPPV) must be designed to provide a P_{delta} of at least 3% of the $P_{available}$. P_{delta} is the amount of active power used to reduce the available active power to provide a reserve for frequency stabilization. It will be possible to enable and disable the frequency

response control function between F_{min} and F_{max}. The modification must start within two seconds and be finished within ten seconds of receiving the instruction to change the frequency control set point (P_{delta}). The difference in precision between the executed control's precision (change in active power output) and the set point must not exceed +/-2% of the target value or +/-0.5% of the power rating, whichever provides the highest tolerance.

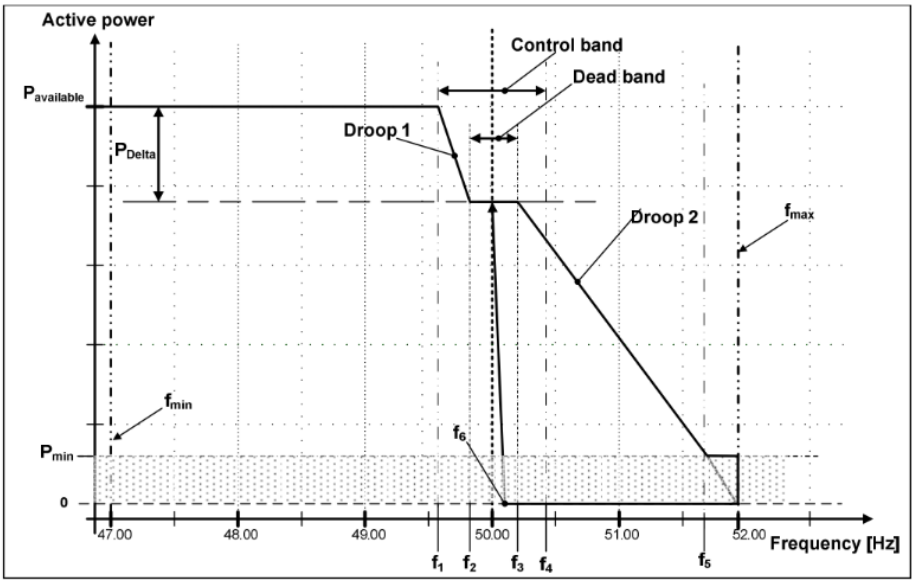

Figure 2.7 Minimum requirements for frequency response of Group C [8].

Unless otherwise agreed upon between the SO and the RDG generator, the default parameters for F_{min}, F_{max}, F_4, F_5 and F_6 shall be as given in Table 2.5. The settings for F_1, F_2 and F_3 must be agreed upon with the SO. .

Table 2.5 Frequency response for RDGs in category C [8].

FREQUENCY	FREQUENCY VALUES
F_{min}	47
F_{max}	52
F_1	As arranged with SO
F_2	As arranged with SO
F_3	As arranged with SO
F_4	50,5
F_5	51,5
F_6	50,2

2.3.4. Reactive power support needs under the grid code

Group B RDGs must be designed to work in voltage (V), power factor or reactive power (Q/Mvar) control modes. The actual operation mode (V, power facto or Q control) and operating point must be agreed upon with the NSP. When operating at 5% to 100% of rated power (MW), the RDG of Group B must be capable of adjusting reactive power support at the POC within the reactive power capability ranges given in Figure 2.8, where Q_{min} and Q_{max} are voltage dependent as defined in Figure 2.9. depicting the needed RDG reactive power capability measured at the POC at nominal voltage. When operating at less than 5% of rated true power, there is no need for reactive power capacity. However, the RDG can only function within the reactive power tolerance range, which cannot exceed +/-5% of rated true power, as shown in Figure 2.9.

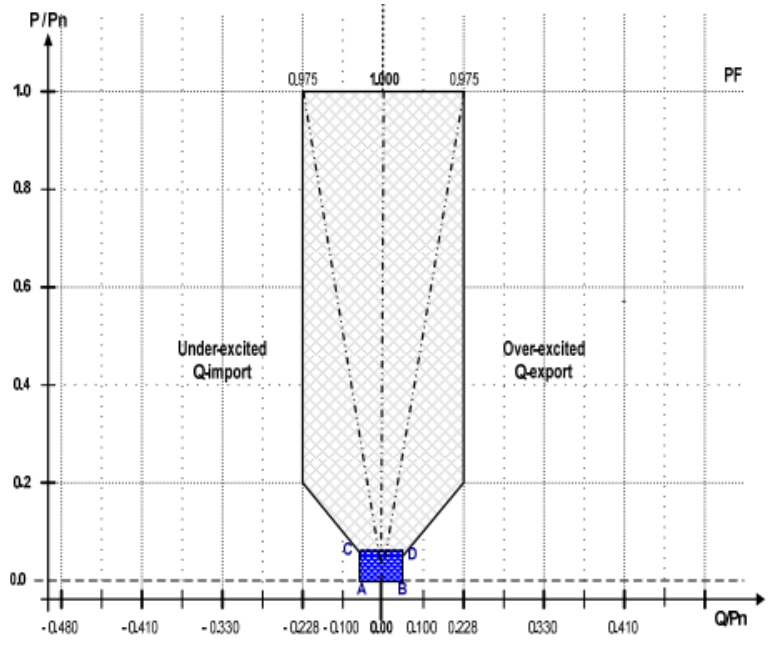

Figure 2.8 RDGs of Group B reactive power requirements [8].

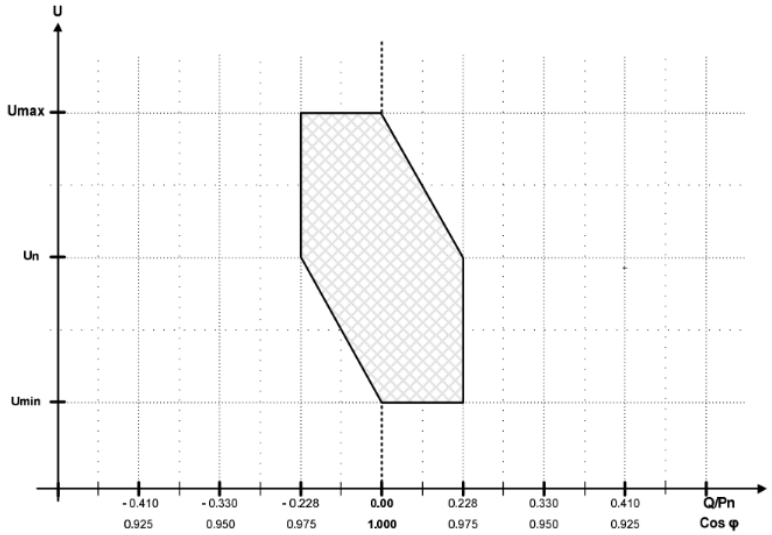

Figure 2.9 Grid code requirements for Group B reactive power and voltage control range [8].

Group C RDGs must be designed to operate in voltage, power factor or reactive power management modes. When operating at 5% to 100% of rated real power, the RDG of Group C must be capable of adjusting reactive power support at the POC within the reactive power capability ranges indicated by Figure 2.10, where Q_{min} and Q_{max} are voltage dependent as defined by Figure 2.11. Figure 2.10 depicts the needed RDG reactive power capability measured at the POC at nominal voltage. When operating at less than 5% of rated power, there is no need for reactive power capacity. However, the RDG can only function within the reactive power tolerance range, which cannot exceed +/-5% of rated active power, as shown in Figure 2.10.

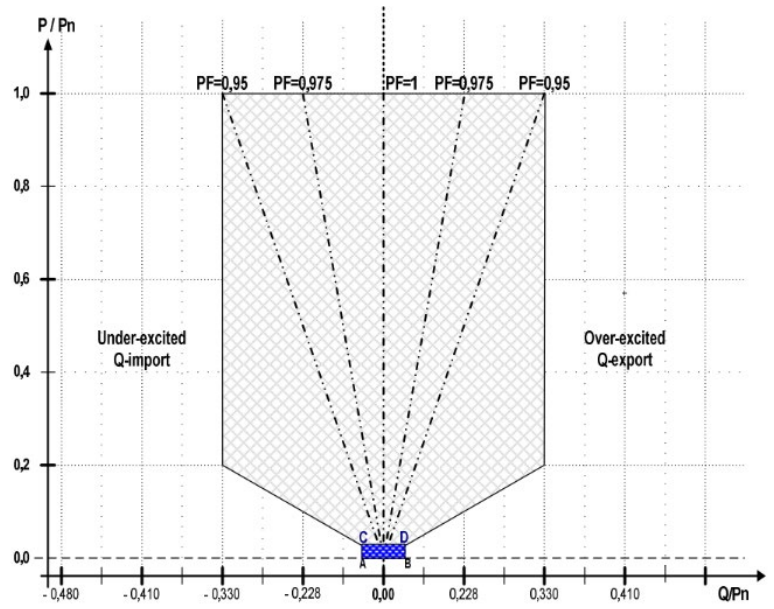

Figure 2.10 RDGs of Group C reactive power requirements at the nominal voltage in the point of connection [11].

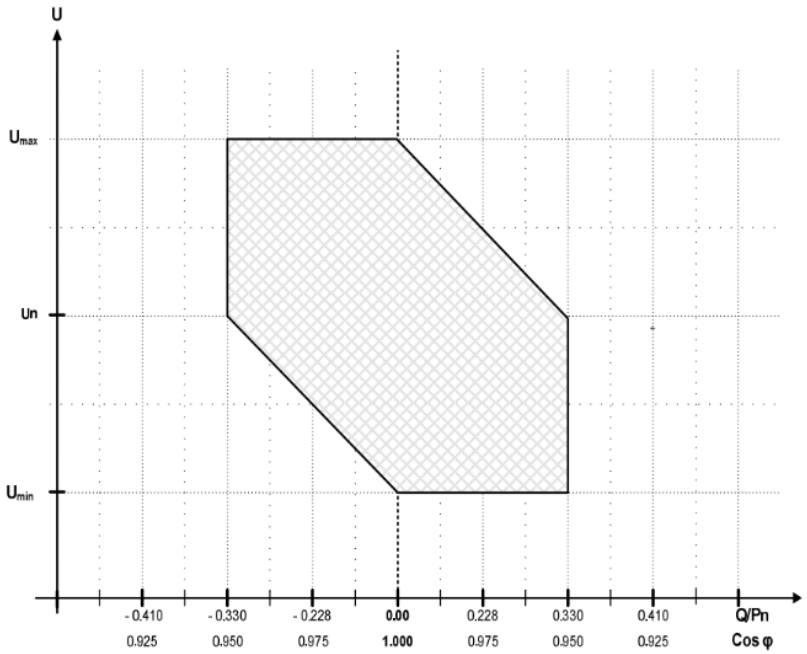

Figure 2.11 RDGs of Group C reactive power and voltage control range requirements [11].

2.3.5. Functions of reactive power and voltage regulation

The RDG must provide reactive power control functions that can control the reactive power supplied by the RDG at the POC, as well as a voltage control function that can control the voltage at the POC via orders using set points and gradients. Since the

reactive power and voltage control functions are mutually exclusive, only one of the three functions listed below can be activated at a time:

- Voltage Control.
- Power Factor Control; and
- Q Control.

The NSP, in collaboration with the SO, should specify the control function and apply parameter settings for reactive power and voltage control functions that will be implemented by the RDG generator. The operating agreement must include documentation of the agreed-upon control functions.

a. Control of reactive power

To regulate the flow and absorption of reactive power at the POC, Q control is a control function that acts independently of active power and voltage. In Figure 2.12, this control function is depicted as a vertical line. If the NSP, SO or their agent modifies the Q control set point, the RDG's echo analogue set point value must be updated within two seconds. Within 30 seconds of receiving an order to change the set point, the RDG will respond to the new set point. The control and set point accuracy shall not exceed +/-2% of the set point value or +/-0.5% of the maximum reactive power, whichever produces the largest tolerance. The RDG must be capable of receiving a Q set point with a minimum precision of 1 kvar [12].

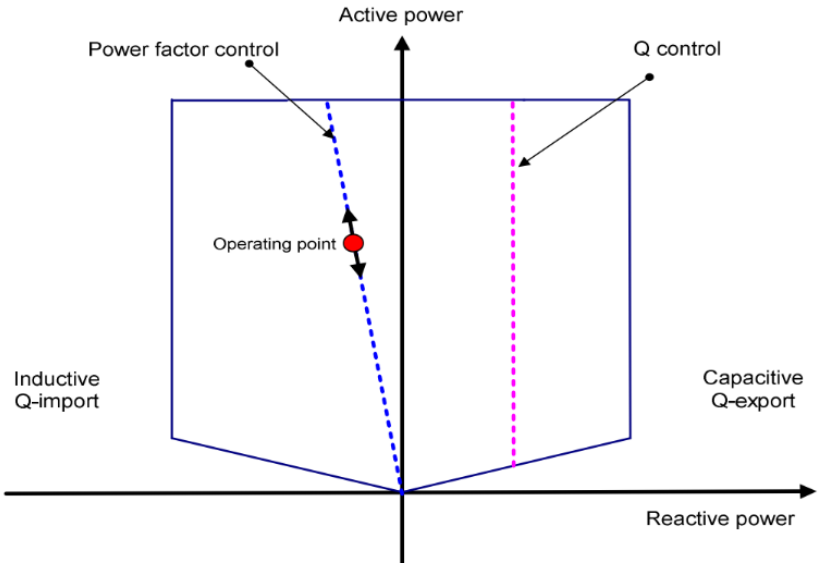

Figure 2.12 Reactive power (Q) control functions [12].

b. Regulation of the power factor

Power factor control is a control function that regulates the reactive power at the POC in relation to the active power. Figure 2.12 depicts this with a line with a constant gradient. If the NSP, SO or their agent changes the power factor set point, the RDG must respond to the new value by updating its echo analogue point setting within two seconds. Following receipt of an instruction to alter the set point , the RDG must respond to the new set point within 30 seconds. The precision of the executed control and the set point shall not deviate by more than +/- 2%.

c. Voltage Regulation

Voltage control is a control function that regulates the voltage at the point of control. If the voltage set point is to be altered, the change must begin within two seconds and be completed within 30 seconds after receiving an order to modify the set point. The accuracy of the voltage set point must be within +/-0.5 percent of the nominal voltage, and the precision of the control must be within +/-2 percent of the required injection or absorption of reactive power, as shown in Figure 2.13. With the droop configured as shown in Figure 2.13, the individual RPP must be able to conduct the control within its dynamic range and voltage limit. Droop is the voltage shift (pu) generated by a change in reactive power in this context (pu). When the voltage control reaches the dynamic design limits of the RDG, the control function

must wait for possible overall control from the tap changer or other voltage control functions. The NSP, in partnership with the SO, will be in charge of overall voltage coordination[12].

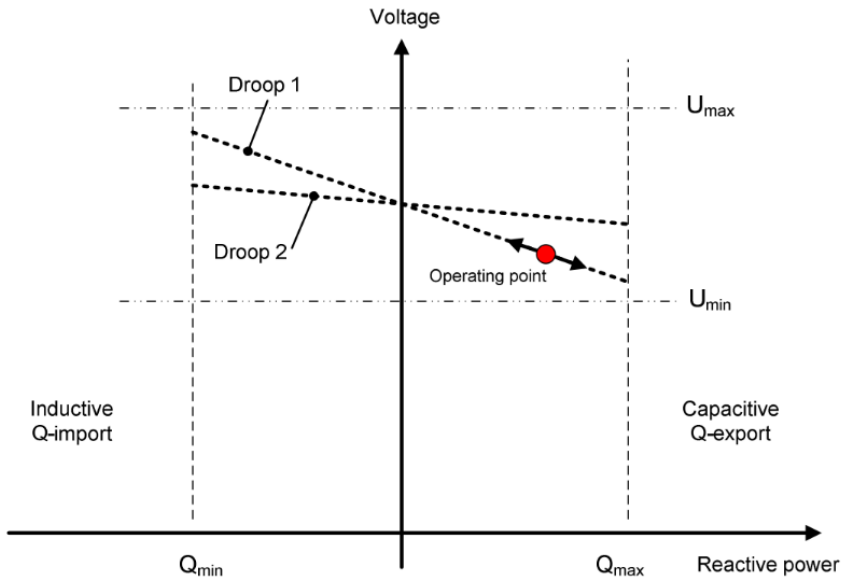

Figure 2.13 RDG voltage control [12].

2.4. Summary

This chapter has covered the technical requirements for distributed generators connected to the grid, as well as their classes.

CHAPTER 3:

REVIEW OF WIND ENERGY CONVERSION SYSTEM TECHNOLOGY AND CONTROL METHODS

3.1. INTRODUCTION

This chapter emphasizes the fundamental wind turbine characteristics as well as its structure, which are critical for turbine controller design. Thereafter, a brief introduction to wind turbine technology is offered, with an emphasis on energy conversion. Furthermore, several control systems for a double-fed induction generator proposed by different authors have been discussed.

3.2. Wind Turbine Technology

Wind turbines are available in a variety of sizes, ranging from a few kilowatts for residential or commercial use to several megawatts for large wind farms. Small-to-medium-sized wind turbines typically have a capacity of less than 300 kW and can be installed at homes, farms, and businesses to offset utility power consumption. Small wind turbines can be combined with other energy sources such as photovoltaic panels and diesel generators to create a self-contained/off-grid generation system for remote areas where access to the power grid is difficult or prohibitively expensive. On the other hand, the size of large wind turbines has continued to grow in recent years. Increased wind turbine size results in increased output power as energy captured is proportional to the square of the rotor radius. This can be seen by relating the rotor diameter and tower height to the wind turbine's power rating, as illustrated in Figure 3.1.

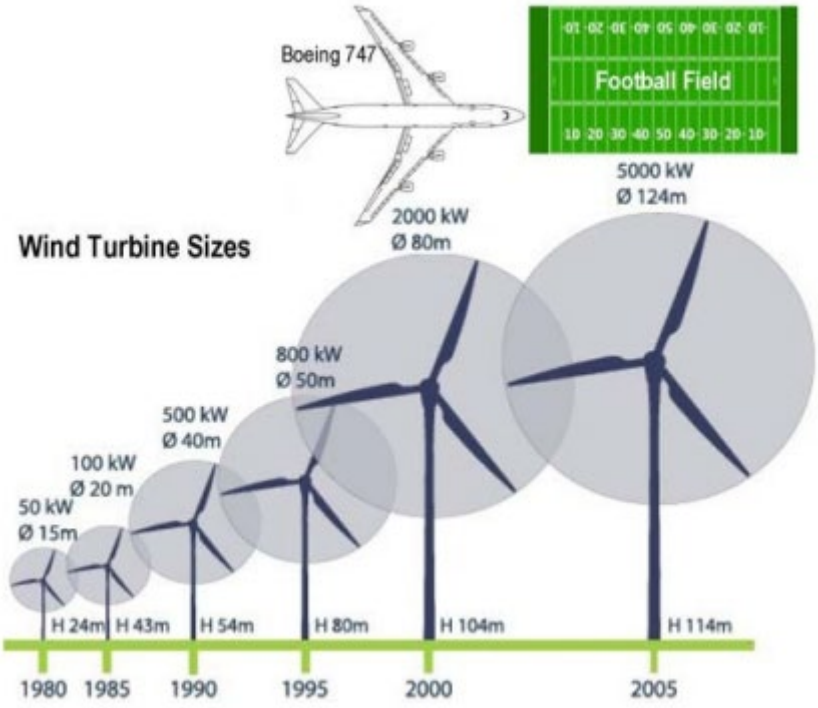

Figure 3.1 Evolution of wind turbine size [13].

3.2.1. Offshore and on-land Applications

Historically, large-scale wind farms have been located on land for a variety of reasons, including ease of construction, low maintenance costs, and proximity to transmission lines. Offshore wind farms, on the other hand, are commercially viable. One of the primary reasons for the development of offshore wind farms is a lack of suitable wind resources on land. This is especially true in densely populated areas, such as those found in several European countries. Another significant reason is that offshore wind is frequently significantly stronger and more consistent than wind on land. Given that the energy produced by wind turbines is proportional to the cube of the wind speed, the environmental impact in offshore applications, such as audible noise and visual impact, is negligible. These factors are the primary drivers of offshore wind turbine technology development. While offshore wind turbine prototypes can be found worldwide, only a few countries (mostly in Europe) have operational offshore wind farms. The total installed cost of on-land and offshore wind energy systems is depicted in Figure 3.2 [14].

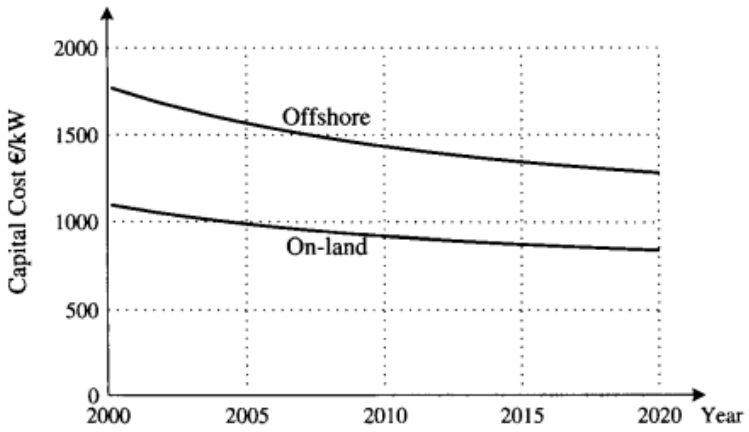

Figure 3.2 Comparison of total installed cost for on-land and offshore wind energy system [14].

3.2.2. Vertical and Horizontal – Axis Wind Turbines

Wind energy is one of the most environmentally friendly and widely used forms of renewable energy. Wind farms are South Africa's largest source of renewable energy and are classified into two types: Vertical Axis Wind Turbines (VAWT) and traditional Horizontal Axis Wind Turbines (HAWT). Figure 3.3 illustrates both VAWT and HAWT-axis wind turbines [14].

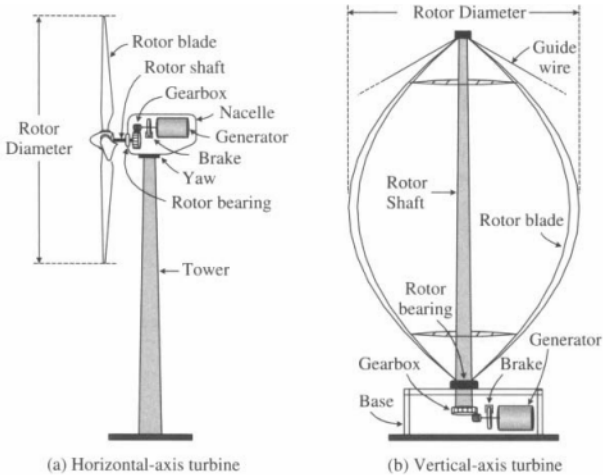

Figure 3.3 Vertical and Horizontal - axis wind turbines [14]. .

The spin axis of horizontal-axis wind turbines is parallel to the ground, as illustrated in Figure 3.3a. The tower lifts the nacelle to create enough room for the rotor blade movement and to take advantage of favourable wind conditions. The nacelle houses

the gearbox, generator and, in some circumstances, power converters. The industry-standard HAWT is equipped with a three-bladed rotor mounted in front of the nacelle, a configuration referred to as the "upwind configuration". However, realistic uses include downwind arrangements with the blades towards the back. On wind farms, turbines with one, two or more than three blades are also common. The spin axis of vertical-axis wind turbines is perpendicular to the ground. Turbine rotor blades are made up of curved vertically mounted air foils. Typically, the generator and gearbox are mounted on the ground near the base of the turbine, as illustrated in Figure 3.3b. The VAWT's rotor blades come in a range of forms and configurations. The design depicted in Figure 3.3b is a popular one. Generally, the VAWT requires guide wires to maintain the rotor shaft in a constant position and to limit mechanical vibrations. Table 3.1 compares the HAWT and VAWT [14]. .

Table 3.1 Comparison between vertical and horizontal axis wind turbine [14].

Turbine Type	Advantage	Disadvantage
HAWT	• Increased efficiency of wind energy conversion. • Due to the tower's height, it has access to stronger winds. • At high wind speeds, power regulation is accomplished through stall and pitch angle control.	• Costlier installation, stronger towers to support the nacelle's heavy weight. • Increased cable length from the top of the tower to the ground. • Yaw control required.
VAWT	• Due to the ground-level gearbox and generator, installation costs are reduced and maintenance is simplified. • Operation is not dependent on the direction of the wind. • Appropriate for rooftops (strong wind without the need for a tower).	• Wind energy conversion efficiency is reduced. • Increased torque fluctuation and susceptibility to mechanical vibrations. • At high wind speeds, power regulation options are limited.

Numerous researchers have lost interest in vertical axis wind turbines due to their inability to generate large amounts of electricity on a large scale. Whoever, this method appears to be a viable option in urban areas where the traditional method is ineffective. Thus, the design of VAWT is critical to gradually increase wind energy penetration in towns and cities. Since VAWTs are bi-directional, they can capture wind energy in all directions without the assistance of additional technology such as a yawing mechanism. Additionally, it is much easier to maintain the generator and gearbox. The blades of traditional horizontal axis wind turbines are parallel to the ground. These models have garnered increased attention due to their higher energy generation efficiency when compared to vertical axis wind turbines. Even though these wind turbines generate more energy, they can only extract wind energy in one direction and operate at a low rotor speed. As a result, a transmission system is required to match the rotor speed of the wind turbine to the generator speed [14].

3.2.3. Variable and Fixed Speed Turbines

Additionally, wind turbines can be classified as fixed-speed or variable-speed. As the name implies, fixed-speed wind turbines spin at a nearly constant speed determined by the gear ratio, grid frequency, and number of generator poles. Maximum conversion efficiency is only possible at a particular wind speed, and system efficiency degrades at other wind speeds. The turbine is protected from damage caused by high wind gusts of the aerodynamic control of the blades. Fixed-speed turbines deliver highly fluctuating output power to the grid, causing power system disruptions. Additionally, this type of turbine requires a robust mechanical design capable of withstanding high mechanical stresses. Variable-speed wind turbines, on the other hand, can maximize energy conversion efficiency over a wide range of wind speeds. The turbine's rotational speed can be continuously adjusted in response to the wind speed. Thus, the tip speed ratio, defined as the ratio of the blade tip speed to the wind speed, can be maintained at an optimal value to maximize power conversion efficiency across a range of wind speeds [15].

Wind turbine generators are typically connected to the utility grid via a power converter system to allow for variable turbine speed. The transmission system enables the wind

turbine's generator to be mechanically coupled to the rotor. As illustrated in Table 3.3, the variable-speed turbine's primary advantages include increased wind energy output; improved power quality; and decreased mechanical stress. The primary disadvantages are increased manufacturing costs and power losses caused by power converters. Nonetheless, the increased cost and power losses are offset by the controlled generator, which alleviates mechanical stress on the turbine, drive train and supporting structure. This has enabled manufacturers to develop more cost-effective large wind turbines. Due to the foregoing, variable-speed turbines currently dominate the market [14].

Table 3.2 Comparison of fixed wind turbine and variable speed wind turbine [14].

Speed Mode	Advantages	Disadvantages
Fixed speed	• Simple, expendable, and robust. • Low-cost and easy-to-maintain.	• Energy conversion efficiency is relatively low. • Mechanically demanding. • Significant fluctuations in the grid's power supply.
Variable speed	• High efficiency of energy conversion. • Superior power quality. • Mechanical stress is reduced.	• Additional costs and losses are incurred because of converters. • Control systems that are more complicated.

3.2.4. Variable Wind Speed Wind Turbine Technologies

a. Variable-speed wind energy system with synchronous generator

Synchronous generation (SGs) is a well-established technology in variable-speed energy conversion systems (WECS). There are a variety of alternative designs, including permanent magnet and wound rotor generators, salient and no salient pole generators, and external and internal rotor generators. With power ratings ranging from a few kilowatts to a few megawatts, synchronous generators offer a high degree

of adaptability for meeting the diverse technical requirements of practical wind energy systems. Synchronous generators can be built in large numbers and operate at a speed that is identical to that of the turbine blades. A direct-drive system eliminates the need for a gearbox [14] . This results in lower installation and maintenance costs and gives the turbine an advantage over induction generator (IG)-based turbines, which requires the use of a gearbox. Normally, the SG wind energy system is controlled by full-capacity power converters operating at variable speeds, ensuring maximum wind energy conversion efficiency throughout its operating range. The system's full-capacity converters enable it to comply with various grid codes, including leading/lagging reactive power control and fault ride-through operation, without requiring additional equipment [14].

b. Variable-speed wind energy system with Induction generator

In the wind energy business, there are two primary types of induction generators: doubly fed induction generators (DFIGs) and squirrel-cage induction generators (SCIGs). These generators share a common stator structure and only differ in their rotor structures. The building of a squirrel-cage induction generator is illustrated in Figure 3.4 [14].

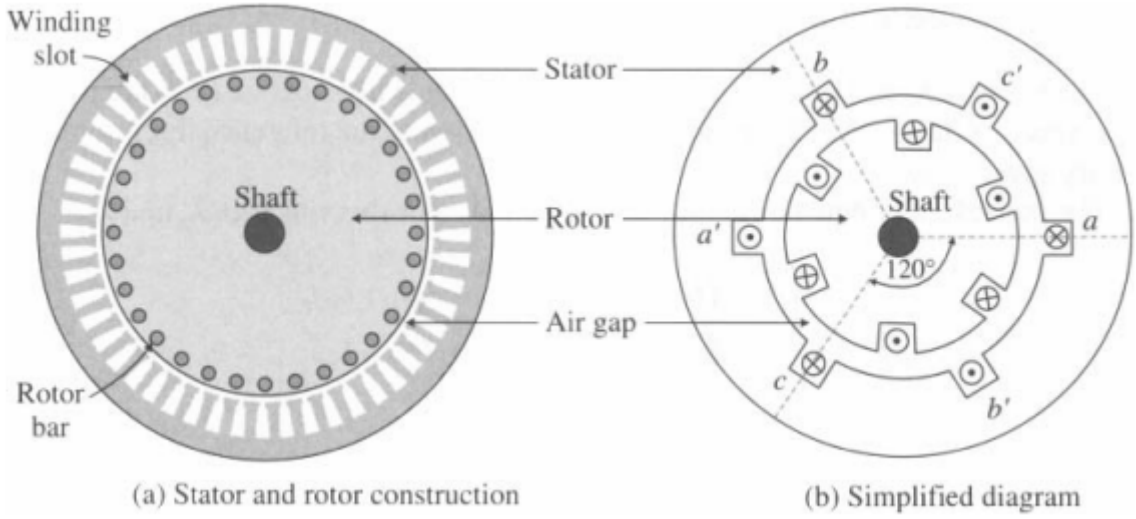

Figure 3.4 SCIG in cross-section [14].

The stator is constructed from extremely thin silicon steel laminations. Laminations are essentially flat rings with openings along their inner perimeter. When the laminations are stacked together with the apertures aligned, a canal is formed for the installation of a three-phase copper winding. The SCIG's rotor is made up of a laminated core and rotor bars. Rotor bars are embedded in slots within the rotor laminations and are terminated with end rings on both ends. When the stator winding is coupled to a three-phase supply, the air gap generates a spinning magnetic field. Induced by the spinning field, a three-phase voltage is generated in the rotor bars. Due to the shorted rotor bars, the induced rotor voltage generates a rotor current that interacts with the rotating field to generate the electromagnetic torque [14].

Similar to the stator winding, the rotor of the DFIG is three-phase wound. The rotor winding is not embedded in the laminations of the rotor but on the outside perimeter. Typically, this winding is fed via slip rings attached to the rotor shaft. The rotor winding is typically coupled to a power converter system that allows for variable rotor speed in the DFIG wind energy system. For the induction generator, there are two widely used dynamic models. The first is based on Space Vector theory, whereas the second is derived from space vector theory via the dq-axis model. While the space vector model employs concise mathematical expressions and a single equivalent circuit, it requires complex (real and imaginary part) variables, whereas the dq-frame model employs two equivalent circuits, one for each axis. These models are inextricably linked and are equally applicable to the investigation of the induction generator's transient and steady-state performance [14].

3.2.5. Power Idiosyncrasy of a wind turbine

The performance and efficiency of the wind turbine is determined by the power curve. This strategy utilizes the relationship of developed horsepower of the wind turbine to the wind speed. Hence, the power curve is the performance nameplate of the wind turbine. The standard IEC61400-12 is utilized to measure the performance of the wind turbine or rating of the wind turbine. Figure 3.5 shows the power curve that is developed based on 3-wind speed conditions, namely cut-in wind speed, rated wind

speed and cut-off wind speed. The wind turbine is expected to start generating power for the grid at cut-in speed and when it reaches cut-off speed, the turbine is expected to stop delivering or generating output power for the grid. The wind turbine is expected to deliver its maximum power at the rated wind speed. The control of wind turbine blades starts when the wind speed reaches the rated speed for protection purposes, and stall and pitch angle control are their popular control strategies [16],[14].

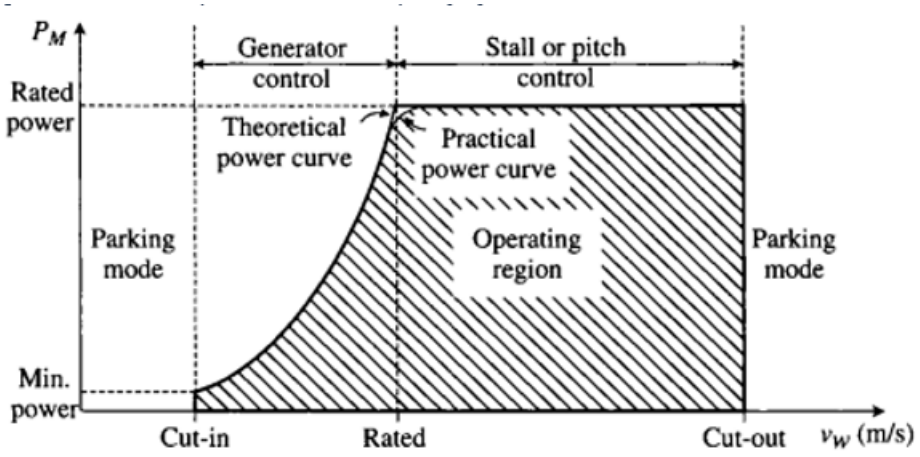

Figure 3.5 Wind turbine power curve [14].

a. Maximum Power Point Tracking

Maximum power point tracking strategy is becoming a trend in many research studies in this modern era [17]. This control technique is more popular in renewable energies, where the primary energy is uncertain. Hence, Mppt provides maximum power available in a fluctuating primary energy source, such as wind energy and solar energy[18]. In wind energy, the Mppt algorithm is applied to extend the harvesting of wind energy by the optimization of the power coefficients during the operations below the rated speed [19]. Hence, the performance of output power of the wind turbine highly relies on the precision of the peak power points that are tracked by the maximum power point tracking controller [20]. According to previous researchers, maximum power extraction algorithms can be classified into three main control groups, namely power signal feedback control, hill-climb search control and tip speed ratio [20].

b. MPPT method using the tip speed ratio control of wind energy conversion systems

The tip speed ratio control strategy regulate the generator rotational speed, in order to achieve the tip speed ratio at its maximum, which matches the maximum power

harvested [21]. For this method to be successfully accomplished, it requires both turbine speed and wind speed to estimate the required maximum tip speed ratio of the wind turbine, for the system to harvest possible maximum power available from the wind. Figure 3.6 below illustrates the diagram of tip speed ratio applied in wind energy conversion systems.

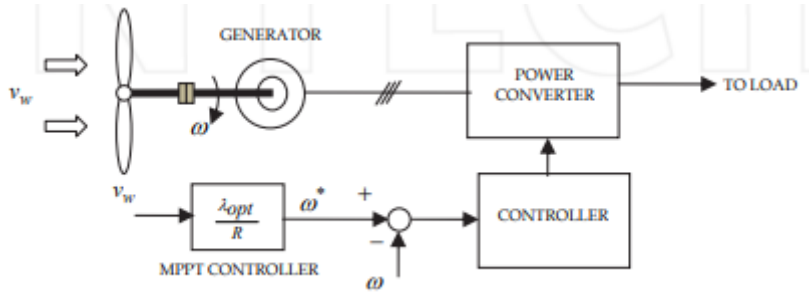

Figure 3.6 Tip speed ratio control of wind energy conversion system [20]. .

c. MPPT method using power feedback control.

The power feedback control is achieved by obtaining the estimated values of the generator speed, and the wind speed is not necessary for this method. However, the characteristics of the wind turbine and generator speed are highly essential. Hence, the wind turbine's maximum power curve is necessary to know, and this curved is tracked based on its mechanism control. In power signal feedback control, power reference is generated by utilising a mechanical power equation or pre-determined maximum power curve. Alternatively, rotor speed might be utilised as the input. This control strategy is categorised into two groups, namely optimum power feedback control and the optimum torque feedback control. Nevertheless, these control strategies are identical. Figure 3.7 demonstrates the optimum power feedback. Figure 3.8 shows the block diagram of optimum torque feedback.

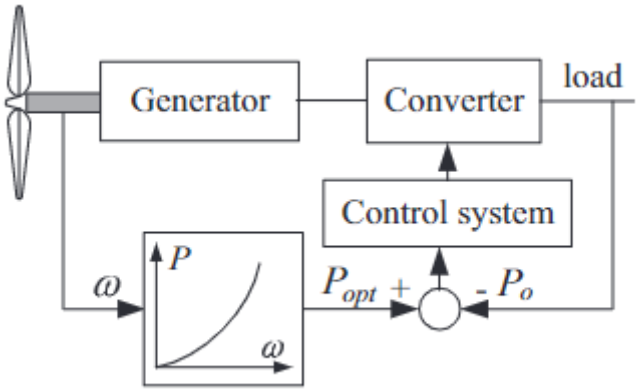

Figure 3.7 Optimum power feedback control [22].

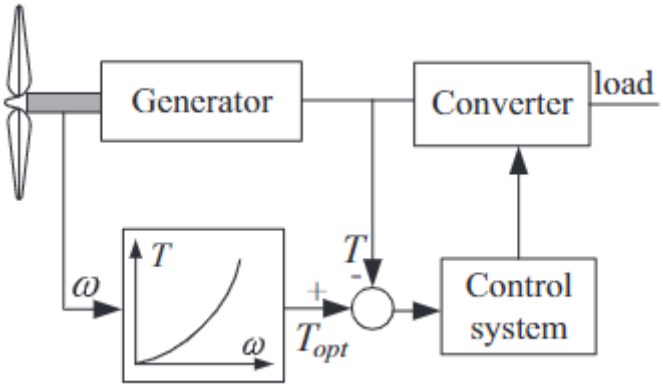

Figure 3.8 Optimum torque feedback [22]. .

d. MPPT method using hill-climb search

This control algorithm uses the strategy of frequently tracking the optimum power of WECS. In [20], hill-climb searches have an advantage of overcoming the difficulties faced by the other two methods, namely power signal feedback control and tip speed ratio control of wind energy conversion systems. The search algorithm relies on the position of the running locus and connection difference between the speed and power. It regulates maximum signal to control the system to its most productive operating point. Figure 3.9 demonstrates the control principle of the hill-climb search strategy and Figure 3.10 shows the hill-climb search applied to the wind turbine.

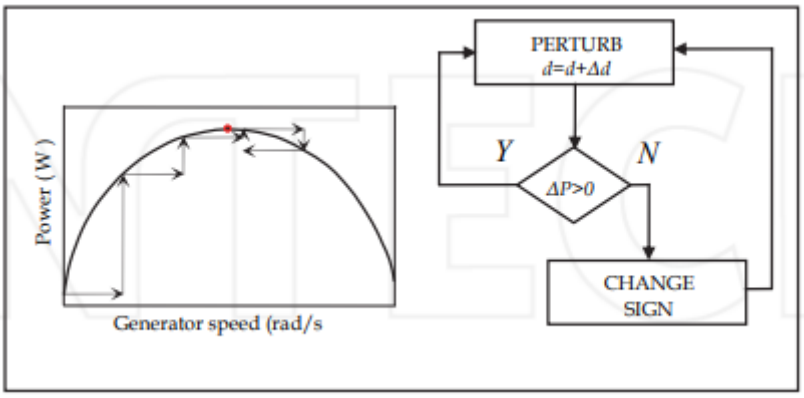

Figure 3.9 HCS control principle [20].

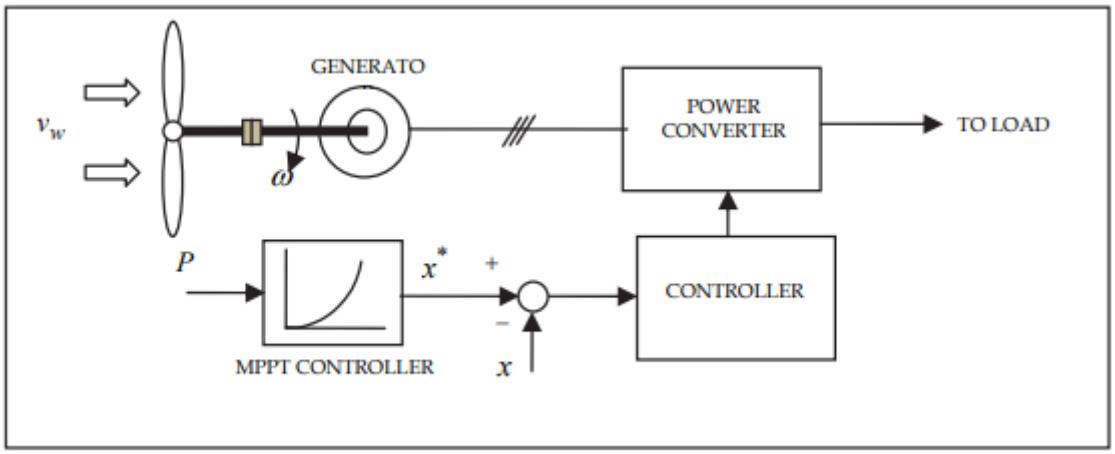

Figure 3.10 Hill-climb search control applied on wecs [20]. .

3.2.6. WECS mechanical transmission models

The mechanical transmission system of WECS consist of two components, namely the gearbox and generator [23]. WECS with three blades typically operate at rotor speeds ranging from 6 to 20 rpm. In comparison to typical generator speed ratings, which may be 1800 or 1200 rpm for a stator frequency of 50 Hz, this speed range is lower. Hence, the transmission system is responsible for matching a low rotor speed with the high-speed generator side. Speed matching is accomplished through the proper design of the gear box conversion ratio between rated rotor blade speed and generator rated speed [16]. Figure 3.11 shows the gearbox of multiple stages of a transmission system. This layout is intended for megawatt WECS. The following equations can be used to develop the gearbox ratio:

$$\gamma_{gb} = \frac{N_m}{N_M} = \frac{(1-S)*50*f_s}{P*N_M} \qquad \textbf{(3.1)}$$

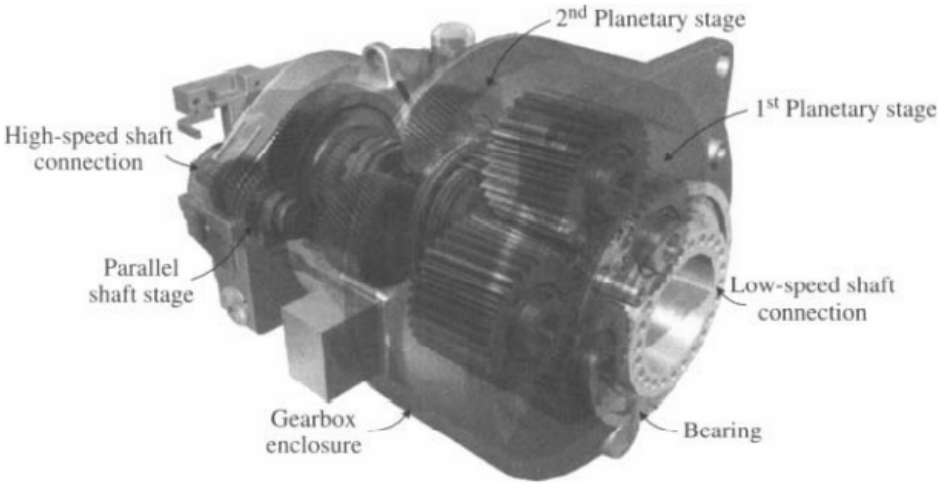

Figure 3.11 Wind turbine gearbox [16].

There different models of drive trains, namely one-mass model, two-mass model, three-mass mode and six-mass model [24].

a. One-mass drive train

The difference of a single-mass drive train is that it is responsible for all moving parts of the wind turbine system. Figure 3.12 shows the diagram of the one-mass drive train. The ratio of motion is given below:

$$2H_{wt} * \frac{d\omega_{wt}}{dt} = T_w - T_G - D_{wt}\omega_t \quad \textbf{(3.2)}$$

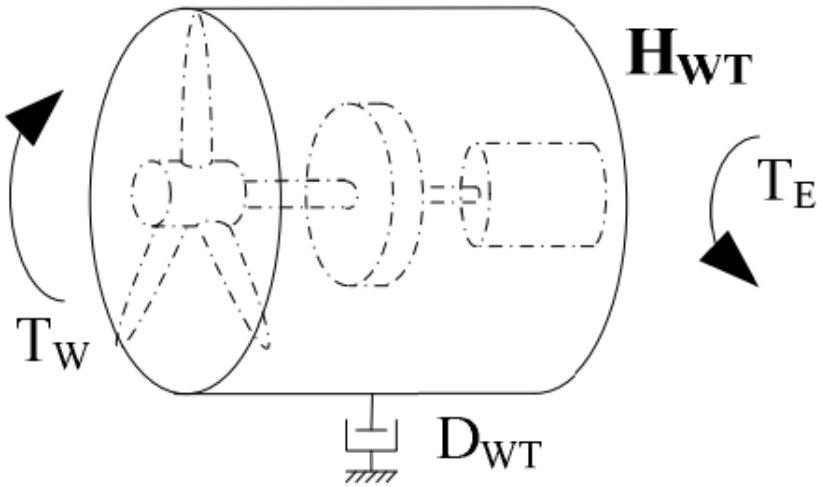

Figure 3.12 Single mass drive train [25].

b. Two-mass drive train

The two-mass drive train is constructed from the three-mass drive train by putting the mass of two plates together. Figure 3.13 demonstrates the block diagram of a two-mass drive train.

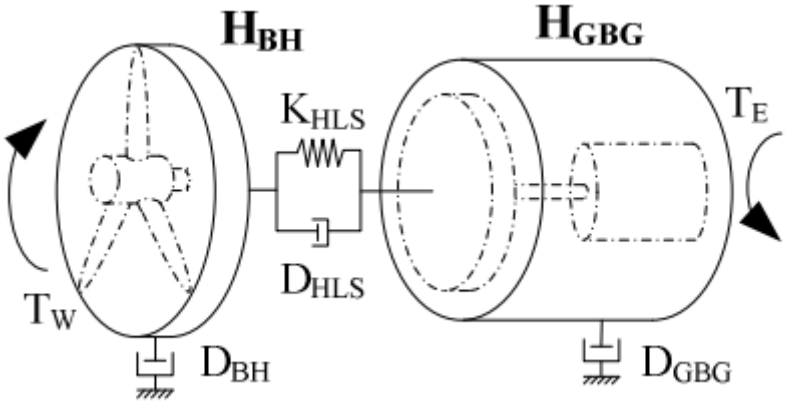

Figure 3.13 Two-mass drive train [25].

Mathematic equations for a two-mass drive train are determined below:

$$K_{HLS} = \left(\frac{{N_{GB}}^2}{K_{HS}} + \frac{1}{K_{LS}}\right)^{-1} \quad \textbf{(3.3)}$$

$$2H_{BH}\frac{d\omega_{BH}}{dt} = T_{\omega} - [K_{HLS} * \theta_{HLS} + D_{HLS}(\omega_{BH} - \omega_{GBG})] - D_{BH} * \omega_{BH} \quad \textbf{(3.4)}$$

$$2H_{GBG}\frac{d\omega_{BH}}{dt} = [K_{HLS} * \theta_{HLS} + D_{HLS}(\omega_{BH} - \omega_{GBG}) - D_{GBG} * \omega_{GBG} - T_G] \quad \textbf{(3.5)}$$

$$\frac{d\theta_{HLS}}{dt} = \omega_0(\omega_{BH} - \omega_{GBG}) \quad \textbf{(3.6)}$$

c. Three-mass drive train

Figure 3.14 illustrates the block diagram of a three-mass model drive train. The inertia of a wind generator could be determined in this model by adding the masses of three blades and the hub. Hence, the mutual damping between blades and hub is neglected. For simplicity purposes, the weight of three-blades is assumed to be uniform.

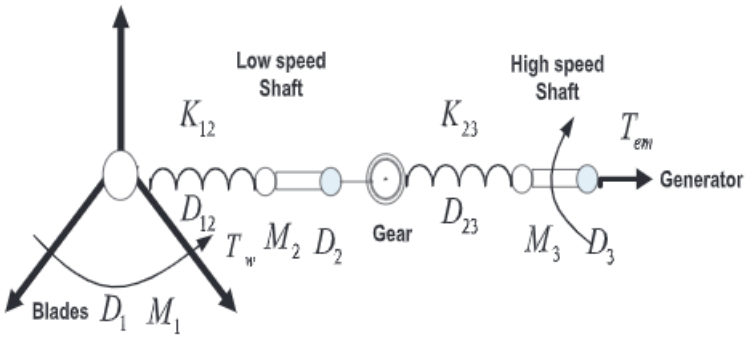

Figure 3.14 Three-mass drive train model [26]. .

The three-mass drive train is categorised into two groups, namely 3-mass type 1, and 3-mass type two. Figure 3.15 indicates a 3-mass type one and Figure 3.16 shows a diagram of a 3-mass type 2.

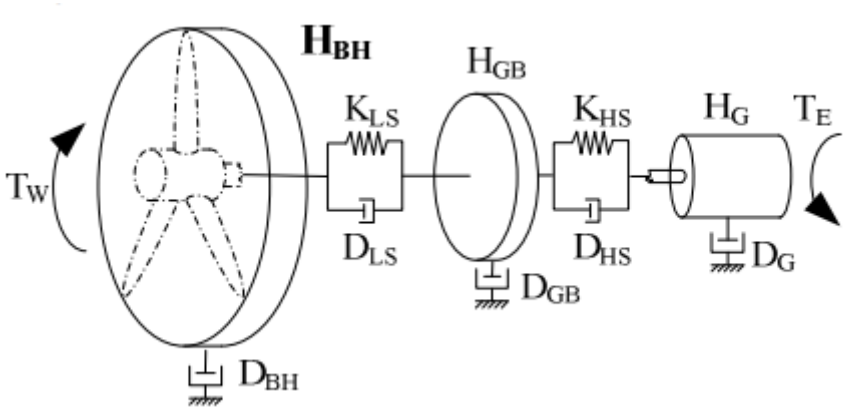

Figure 3.15 Three-mass type 1 [25]. .

Mathematical equations of motion for type-1 are shown below:

$$2H_{BH}\frac{d_{WBH}}{dt} = T_w - [K_{LS} * \theta_{LS} + D_{LS}(W_{BH} - W_{GB})] - D_{BH} * W_{BH} \quad \textbf{(3.7)}$$

$$2H_G\frac{d_{wg}}{dt} = [K_{HS} * \theta_{HS} + D_{HS}(W_{GB} - W_G)] - D_G * W_G - T_G \quad \textbf{(3.8)}$$

$$\frac{d\theta_{LS}}{dt} = W_0(W_{BH} - W_{GB}) \quad \textbf{(3.9)}$$

$$\frac{d\theta_{HS}}{dt} = W_0(W_{GB} - W_G) \quad \textbf{(3.10)}$$

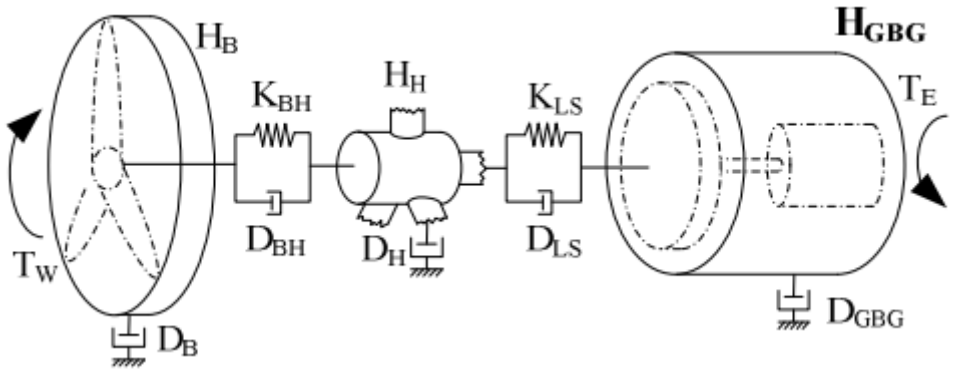

Figure 3.16 Three-mass type-2 [25]. .

Equations of motion for type-2 are determined below:

$$2H_B \frac{d_{\omega b}}{dt} = T_W - [K_{BH} * \theta_{BH} + D_{BH}(\omega_B - \omega_H)] - D_B * \omega_B \quad \textbf{(3.11)}$$

$$2H_H \frac{d\omega_H}{dt} = [K_{BH} * \theta_{BH} + D_{BH}(\omega_B - \omega_H)] - [K_{LS} * \theta_{LS} + D_{LS}(\omega_H - \omega_{GBG})] - D_H * \omega_H$$

(2.25)

$$2H_{GBG} \frac{d_{\omega gbg}}{dt} = [K_{LS} * \theta_{LS} + D_{LS}(\omega_H - \omega_{GBG})] - D_{GBG} * \omega_{GBG} - T_G \quad \textbf{(3.12)}$$

$$\frac{d\theta_{BH}}{dt} = \omega_0(\omega_B - \omega_H) \quad \textbf{(3.13)}$$

$$\frac{d\theta_{LS}}{dt} = \omega_0(\omega_H - \omega_{GBG}) \quad \textbf{(3.14)}$$

d. Six-mass drive train

Figure 3.17 shows the block diagram of a six-mass model drive train. This model consists of six inertias, namely gearbox inertia, generator inertia, hub inertia, and each blade have its own inertias for a three-blade wind turbine.

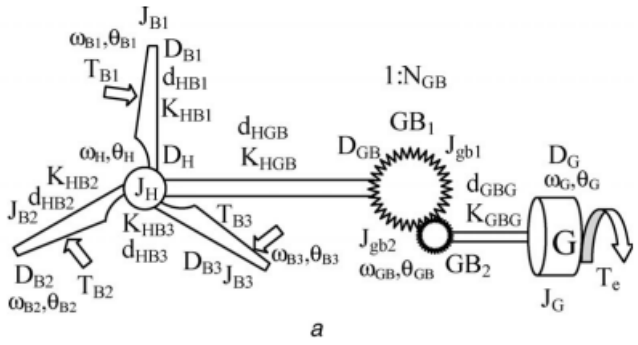

Figure 3.17 Six-mass drive train model [27].

3.2.7. Power Converter for WECS

In wind energy conversion systems (WECS), power converters are frequently employed. In fixed-speed WECS, the converters are used to minimize in-rush flow and torque fluctuations at boot up, but in varying WECS, they modify the generator's speed and torque, as well as active and reactive electricity to a grid. [28]. Ranges of power converter topologies are available for the optimal control of wind energy systems, depending on the system power rating and kind of wind turbine. Voltage source converters (VSCs) or current source converters (CSCs) can be used.

a. AC Voltage Regulators (Soft Starters)

With the rapid growth of renewable energy sources, energy storage systems and high voltage direct current transmission systems, three-phase voltage source converters are being integrated into modern power grids in significant numbers [29]. However, this may introduce novel sorts of instability events associated with VSCs that can arise in current power grids [30], and are not classified as well-defined power system stability problems [31]. Grid synchronization instability is a type of new instability phenomenon that can occur when VSCs with conventional phase locked loops (PLL) are connected to weak grids with high grid impedance. Because VSCs' traditional stable power control mechanism may result in poor frequency control and voltage support capabilities, their increasing utilization poses issues for electric utilities [32]. P-f and Q-V sag management, as well as virtual synchronous machine (VSM) regulation, were developed for usage in VSCs to provide main frequency control and voltage stability for power systems that are either weak or dominated by VSCs [33],[34]. A grid-connected two-level voltage source converter with an inductive filter is illustrated in Figure 3.18.

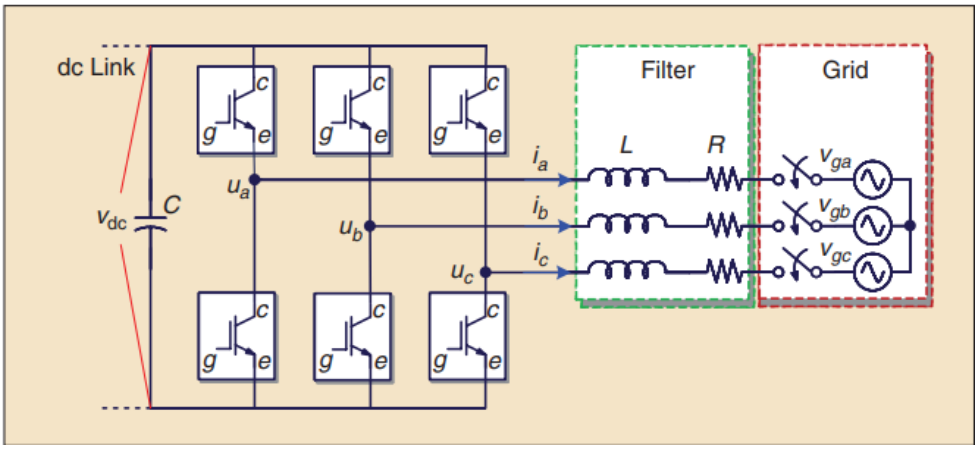

Figure 3.18 Grid connected voltage source converter [35]. .

The AC voltage controller is frequently referred to as a "soft starter" in WECS since its primary purpose is to assist the wind turbine in starting smoothly and with little in-rush current and mechanical stress [36]. Following the system start-up, the AC voltage controller is often bypassed through a bypass switch which eliminates the controller's power losses. AC voltage controllers in WECS are often implemented using an SCR as the switching device. The delay (firing) angle control for SCRs allows the controller's output voltage to be adjusted from zero to its supply voltage, effectively reducing the system's starting current.

b. PWM Current Sources Converter

While voltage source converters (VSCs) generate a defined three-phase PWM output voltage waveform, current source converters generate a defined PWM current waveform [37]. The PWM current source converter is characterized by a straightforward converter design, almost sinusoidal waveforms, and dependable short-circuit safety. It is especially well-suited to high-power applications such as megawatt variable speed drives and wind energy conversion systems. The block diagram in Figure 3.19 depicts a DFIG-based wind turbine with a current source converter.

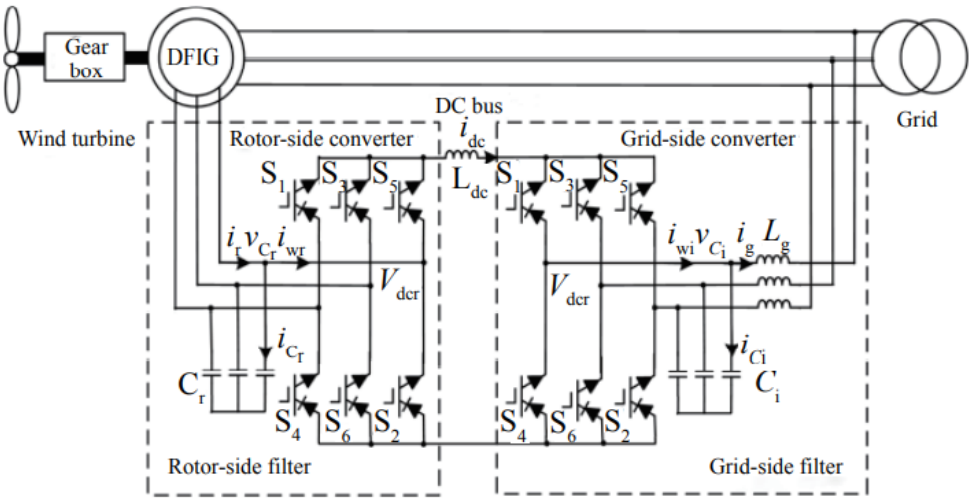

Figure 3.19 DFIG-based wind turbine equipped with current source converter.

A three-phase capacitor is typically required at the output of a current source inverter to assist in the commutation of the switching devices. The capacitor functions as a harmonic filter, enhancing the waveforms of the load current and voltage. The inductor on the DC side of the current source converter provides the implementation of open-loop current management, which enables the bridges to prevent short circuits, and the system configuration demonstrates a high degree of robustness and a flexible strategy for paralleled converters. However, this converter exhibits total harmonic distortion (THD) [38]. The author [39] proposed a new space vector modulation technology that combines space vector modulation with synchronous optimal pulse width modulation, resulting in a system that not only performs well dynamically, but also has a low total harmonic distortion. Based on interconnectivity and damping assignment, author [40] proposes a passive-based control technique for CSC that has good anti-interference capability against load disturbances.

3.2.8. Control strategies of Doubly Fed Induction Generators

Wind farms have become a trend in renewable energy because of their ability to produce large-scale power. Hence, increasing the number of wind farms will uplift the South African economy in the next five years [41]. Additionally, this method of generation is flexible in both rural and urban areas. The penetration of wind power to the distributed generation network is growing exponentially in power networks. South

African grid code requires wind turbines not only to supply active power, but also to provide reactive power support during grid faults until voltage dips are cleared. DFIG has become a trend in wind energy because of it feasibility speed control, power control, smaller converter capacity and improved power quality and system stability [42]. The DFIG system is equipped with bi-directional inverters, providing flexibility to a system of independent controlling active and reactive power [43]. In South Africa voltage fluctuation is a key challenge facing the interconnected network, and this can be shortly explained as a weak grid [44, 45]. Hence, DFIG is capable of supplying or drawing reactive current to or from the power system to improve system stability. However, optimal control strategies are required to perform reactive power injection or absorption control. Hence, balancing reactive power is one of the key responsibilities of RDGs in order to sustain system stability [46].

In [47], the author has performed research on doubly fed induction generator based wind turbines. The challenge of DFIG is performing control in active and reactive power. A comparison of two different control methods has been conducted by author. The author has performed an investigation into DFIG performance under PI controller and sliding mode control. For a PI control, the compensation method was conducted to avoid the zero of transfer function. According to an author [47], and simulation results, the system performance is more robust tin sliding mode control. Moreover, the controller provides reduced settling time, limited peak overshoot values and minimizing oscillations in a short period. The results were obtained in Matlab/Simulink. In [48], the authors have achieved better results with DFIG control utilizing Matlab/Simulink software. To obtain these results, the author used a feedback technique to overcome generator oscillation problems. Furthermore, the feedback control technique was utilized to control power flow between the grid and doubly fed induction generator. This was achieved by using the voltage vectors strategy on the rotor side control.

Indirect vector control (IVC) utilizing proportional-integral regulators is treated as a traditional control system utilized to control DFIG-based wind turbines. However, this technique comes with measure drawbacks such as PI performance is highly reliant on the tuning of parameters and spot-on angular tracking details of stator flux voltage. Additionally, the IVC strategy comes with high harmonic distortions on the rotor current

and power ripples in the DFIG-based wind turbine. Several researchers have studied sliding mode control (SMC) for its high performance and stable control of DFIG. Moreover, this controlling strategy comes with the benefits of quick dynamic response and stability in parameter deviation, and provides excellent performance over non-modelled dynamics. Pulse width modulation (PWM) is a popular control strategy utilized to control ac machines, where the frequency and stator voltage can be maintained with little online computational requirements. This strategy comes with the benefits of being less complex and easier to implement. Notwithstanding the beauty of less complexity and easy implementation, this strategy comes with more total harmonic distortion (THD) in the system. System Space Vector Modulation (SVM) has become a trend on DFIG-based wind turbines because of its capabilities in minimizing the total harmonic distortion of stator current and providing 0.15 times output voltage compared to the PWM. Nevertheless, SVM provides current ripples.

Switching power converters are becoming a trend in industrial applications for fulfilling sufficient energy required by the motor or load. Hence, improved solid-state power equipment and microprocessors are the greatest factors driving the acceleration of switching power converters. Moreover, Pulse Width Modulation is becoming a trend in many power industrial uses that demand high performance [49]. PWM is regarded as the easiest method to control DFIG. When a PWM signal is sent to the power transistor gate, it develops an interval of on and off states for the transistor to deviate from one pulse width modulation period to a second pulse width modulation period relative to the same modulating signal. However, the frequency of the pulse width modulation signal should be in greater quantity than the modulating signal. Hence, the motor/generator relies on the modulating signal. Notwithstanding its attractiveness in providing fewer power losses, easy implementation, less temperature deviation, obtaining output voltage control without additional components, this technique provides total harmonic distortion in the system. However, this can be mitigated by utilizing filters at the lower requirement. The most popular method utilized in PWM scheme voltage sources inverters is sinusoidal PWM. In addition, other techniques are Multiple Pulse Modulation and Single-Phase Modulation.

Single Pulse Width Modulation provides the single alternating pulse per full-half cycle to maintain the output voltage. On the plus side, this is accomplished by connecting the sinusoidal signal to the nil loop, which only accepts the positive component of the reference voltage and outputs a square waveform; and for the negative part of a reference, the signal gives the negative square waveform output signal[50]. In[51], the comparative study of two DFIG control techniques was presented by the author. These two control techniques are space vector modulation and fuzzy pulse width modulation. The results obtained by the author indicated that both control schemes suffer from low power ripples and harmonic distortion if rotor current was reduced. Hence, stator active and reactive power control was achieved. Moreover, the simulations indicated that NSMC control obtained better results compared to NSMC. Hence, third harmonic distortions of rotor currents were reduced in FPWM control. In[52], authors have discussed the contribution of DFIG in power quality and improving transient stability in the interconnected system. Furthermore, this was achieved by controlling reactive power flow between the generator and the grid. Different control strategies were discussed by the author, namely fixed power factor operation; voltage control by rotor excitation; voltage control through grid side converters; and voltage control utilizing both grid side converters and rotor side converters. The author performed simulation results on a Dig silent power factory. In [53], the author has improved the robustness of doubly fed induction generator systems connected into grid. This was achieved by using direct power control and simulated results were obtained by the author. Moreover, the author has conducted simulations under various machine-operating conditions. In [42], authors have performed control of DFIG utilizing an opal-rt real-time simulator in the laboratory. Hence, a laboratory wind turbine emulator for wind energy conversion systems was utilized. The main objective of the author was to keep dc-link voltage constant using a grid side converter and for the rotor side converter, it was possible to control the active and reactive power of the system.

Artificial intelligence techniques have become a trend worldwide and are growing fast. Neural networks, Fuzzy logic and optimization are the most popular artificial intelligent systems. These techniques are more popular because on their ability to handle non-linear plants/models, and robustness of performance even under worse situations. Fuzzy logic has gained much momentum in many research studies as it keeps on

improving its degree of handling system uncertainties. In [54], the major challenges of doubly fed induction generators were handled utilizing a strategy of novel control in conjunction with interval type-2 fuzzy sets [55]. According to the author, the interval type-2 is more robust in handling uncertainties. The author proposed this strategy to improve system stability. According to the author's results, interval type-2 gives improved results compared with type-1 fuzzy logic. In [56], the author has introduced a the new control strategy of controlling DFIG to maximise power generation and supervision of operating stages. The new control scheme strategy was developed for grid synchronization using direct power control. Furthermore, the fuzzy logic controller was introduced by the author to improve system robustness performance under unsteady system parameters. In [57], the author has studied DFIG connected to a national grid subjected to a number of different faults. The author has presented both symmetric and asymmetric faults. Furthermore, the author has studied the control of increased rotor current to prevent increases in DC-link voltage. In addition, the author has proposed the Artificial Neural Fuzzy Inference System to solve the challenge of dc-link voltage increases. In [58], authors proposed fuzzy inference control to replace the traditional controller of a doubly fed induction generator based wind-turbine, known as a proportional and integral (PI) controller. According to the results obtained by the author, the settling time was minimized, oscillations were damped earlier, and no overshooting occurred.

Researchers are developing soft computational techniques to maximize the control of DFIG-based WECS. Hence, the doubly fed induction generator is becoming more popular in renewable energy systems than other renewable types. Recently, researchers have been undertaking a study of merging optimization techniques with artificial intelligent techniques. In [59], the author has proposed the comparison between particle swarm optimization (PSO) based-PID and bacterial foraging optimization (BFO) based-PID. According to an author, the performance of doubly fed induction generators in current, DC-link voltage, terminal voltage and active-reactive power was slightly improved. However, particle swarm optimization provided much improvement compared to the foraging optimization technique. Furthermore, the overshooting of the system was reduced to zero. In [60], the author has proposed a novel grouped grey wolf optimizer to get best parameters for PI controller. Hence,

maximum power point was achieved by the author. Additionally, fault ride-through capability was improved. In [61], authors have used an improved Elman neural network to improve quick and reliable responses in real power control. However, DFIG auxiliary devices are highly sensitive to overcurrent occurrences in the presence of transient disturbances, such as IGBT switches and variable – frequency AC-DC-AC converters. In [62], the author has proposed a differential evolutionary algorithm to mitigate the behaviour of DFIG in the presence of transient disturbances. In [63], the author has proposed a thermal exchange optimization algorithm for PI control tuning to obtain optimal parameters of a PI controller. In [64] and [65], the authors suggested a type-2 fuzzy logic controller to improve system stability under uncertain conditions.

3.3. Summary

This chapter has discussed wind farm technologies and control strategies for DFIG-based WECS.

CHAPTER 4:

MODELLING OF WECS WITH THE CONTROLLER CONNECTED TO GRID

4.1. Introduction

This chapter is concerned with the modelling and simulation of a wind energy conversion system (WECS) rated 1.5 MW mechanical power (a wind farm consist of 3 WECS) that includes a doubly fed induction generator or a permanent magnet synchronous generator (PMSG). A wound rotor induction generator and voltage source converter (VSC) are part of the DFIG-based WECS. The stator side of the DFIG is directly connected to the 25kv, 50 hz power system, but the rotor is partially connected via VSC. The vector control approach is used to regulate WECS reactive power, active power, and dc-link voltage to their nominal values. Furthermore, different control approaches (including fuzzy logic controller, PID controller, and Fuzzy-PID controller) are implemented on the decoupled direct (d) and quadrature (q) axis current loops to keep the active and reactive power (zero Mvar) at their nominal values. For comparison purposes, the identical methodologies used to perform simulations on the DFIG based WECS have been implemented on the PMSG based WECS.

4.2. Modelling of WECS

It is more important to understand the geographic environment since it has a great contribution to wind turbine performance. Hence, the wind turbine's mechanical power performance relies on wind speed. Therefore, it is important to have the geographic information of an area before designing a wind turbine. Table 4.1 shows the climatic data for the Umlalazi area, where the wind farm is expected to be located. Modelling of the WCS can be divided into three stages, namely Aerodynamics, Mechanical and Electrical.

Table 4.1 Umlalazi area climatic data [66].

Month	Temperature (°C)	Humidity (%)	Rain (mm)	Wind (km/h)	Pressure (hpa)
January	24.97	81.46	70.86	23.51	1012.22
February	24.82	78.88	75.6	33.59	1010.33
March	24.08	84.73	79.79	24.31	1010.79
April	22.13	84.54	73.42	23.59	1014.49
May	18.35	86.74	69.36	17.11	1019.10
June	15.77	83.57	30.28	19.06	1018.78
July	14.84	85.71	135.2	20.33	1019.24
August	16.64	81.43	12.29	22.54	1017.94
September	19.67	85.71	123.64	24.06	1015.03
October	20.42	88.88	97.59	21.77	113.29
November	22.22	Na	99.4	31.61	1012.43

4.2.1. Aerodynamics

This work provides an aerodynamic model based on the aerodynamic power coefficient (C_p). For a given rotor, the power coefficient is affected by the pitch angle (β) and the tip speed ratio (λ). Figure 4.1 illustrates the MATLAB/SIMULINK-developed power coefficient as a function of lambda. At maximum C_p, the wind turbine pitch angle is set to zero and it is operating at its rated speed (1.2 pu).

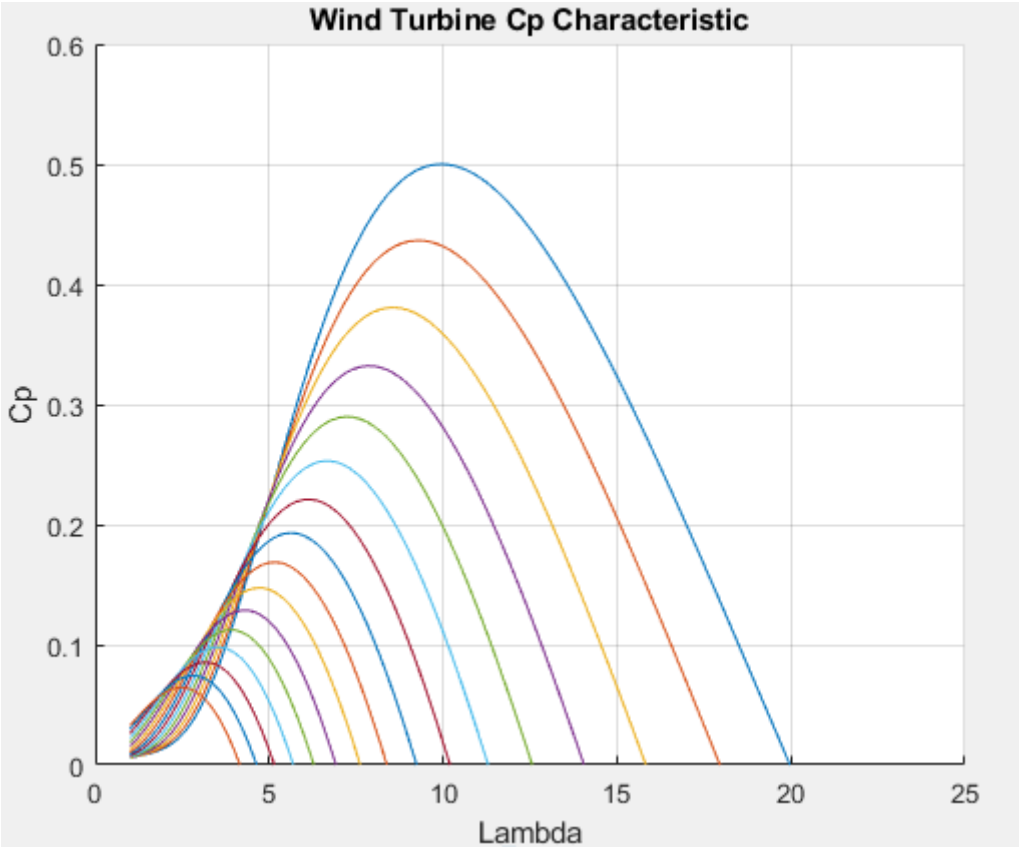

Figure 4.1 Power Coefficient.

The power coefficient represents the power available from the wind and it can be expressed as shown in the following equation:

$$C_p = C_1\left(\frac{C_2}{\lambda_1} - C_3\beta - C_4\right)e^{\frac{C_5}{\lambda_1}} + C_6 \qquad \textbf{(4.1)}$$

Figures 4.2 and 4.3 display the tip speed ratio and CP as wind speed functions respectively.

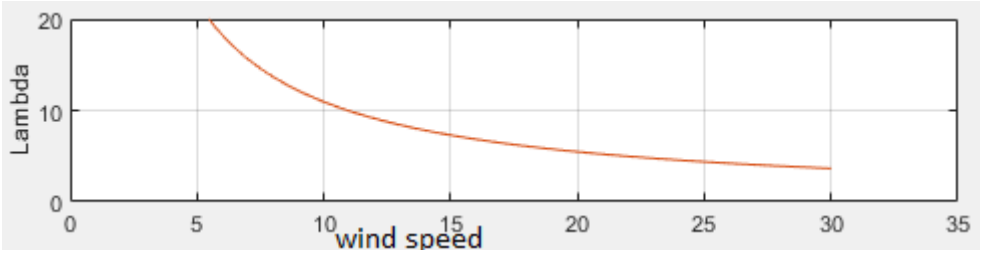

Figure 4.2 Tip speed vs wind speed.

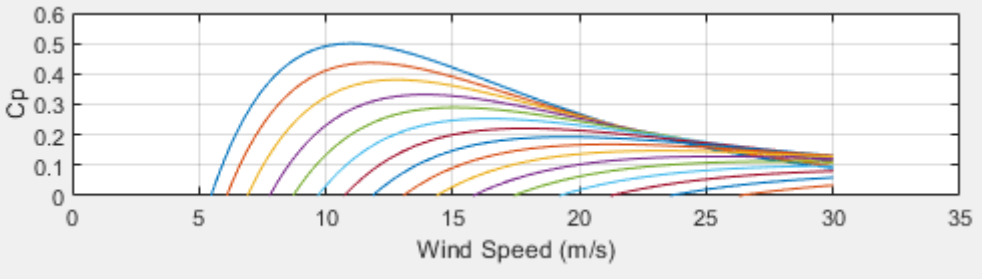

Figure 4.3 Power coefficient vs wind speed.

The tip speed ratio is the difference between rotor speed and wind speed, as described in the following equation:

$$\lambda = \frac{r \times \omega_m}{v} \quad \textbf{(4.2)}$$

The value of λ_1 is determined by the following equation:

$$\frac{1}{\lambda_1} = \frac{1}{\lambda + 0{,}08\beta} - \frac{0{,}035}{\beta^3 + 1} \quad \textbf{(4.3)}$$

4.2.2. Mechanical

The generated output power of a wind turbine is directly proportional to the area of the circumference formed by the blades of a wind turbine as they sweep through the air. Additionally, the cube of the wind speed is directly proportional to the output power of a wind generator. Figure 4.4 illustrates a genetic wind turbine Simulink model. Table 4.2 indicate wind turbine data.

Table 4.2 Wind turbine data.

Number of wind turbine blades	Mechanical power (w)	Nominal wind speed (m/s)
3	1.5×10^6	12

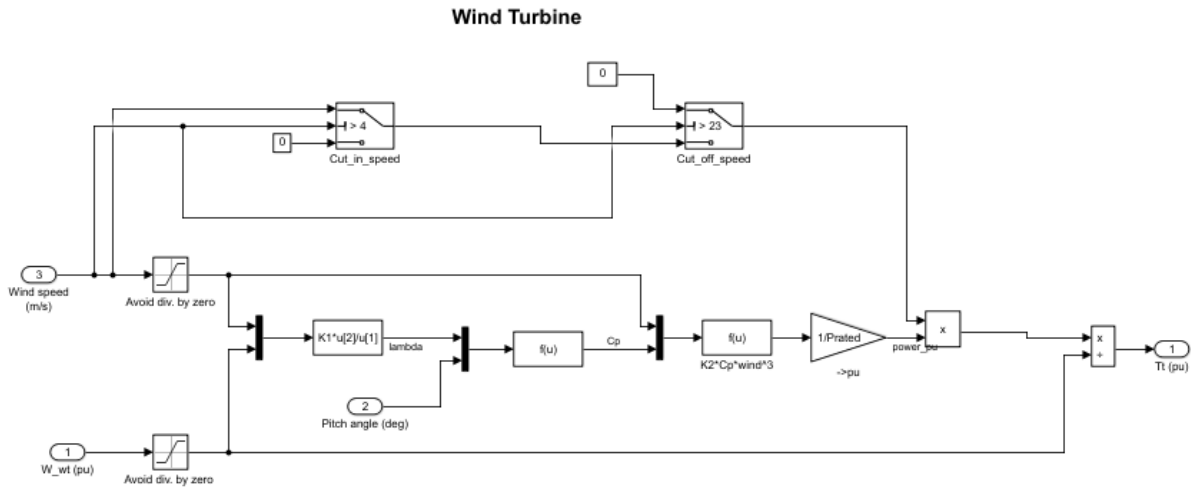

Figure 4.4 Simulink wind turbine model.

The Mechanical Power (P_m) and Mechanical torque (T_m) of a wind turbine are given in the following equations:

$$P_m = \frac{1}{2} \times C_p \times \rho \times A \times v^3 \quad \textbf{(4.4)}$$

$$T_m = \frac{P_m}{\omega} = \frac{1}{2} \times C_p \times \rho \times A \times v^2 (\frac{r}{\lambda}) \quad \textbf{(4.5)}$$

Where: ρ *is air density,* A *area, and* v *is the wind speed.*

The mechanical or drive train model in this work consists of certain aspects of the wind turbine's dynamic structure that have a direct impact on the interaction with power. As a result, the drive train is the only component being studied because it has the most influence on power fluctuations. Other components of the wind turbine, such as the tower and flag bending modes, are overlooked. The drive train model comprises the wind wheel, the turbine shaft (low speed shaft), the gearbox, and the generator's rotor shaft (high-speed shaft). The drive train model is typically represented as a set of masses connected by an elastic coupling with linear stiffness, a damping ratio, and a multiplication ratio. This work is based on a two-mass model. A two-mass model made in MATLAB/SIMULINK is shown in Figure 4.5. Table 4.3 shows the data of the drive train.

Table 4.3 drive train data.

Wind turbine inertia constant (H)	Shaft spring const constant (pu)	Shaft mutual damping (pu)	Turbine speed (pu)
0.42	1.11	1.5	1.2

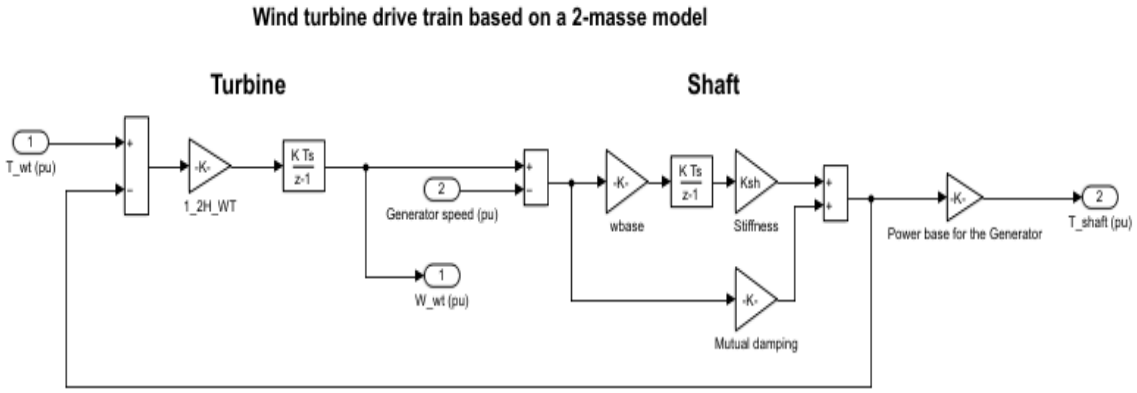

Figure 4.5 Simulink model two-mass drive train.

4.2.3. DFIG-based wind energy conversion system

The control strategy of a DFIG-based WECS is divided into rotor side control (RSC) and grid side control (GSC), as shown in Figure 4.6 below.

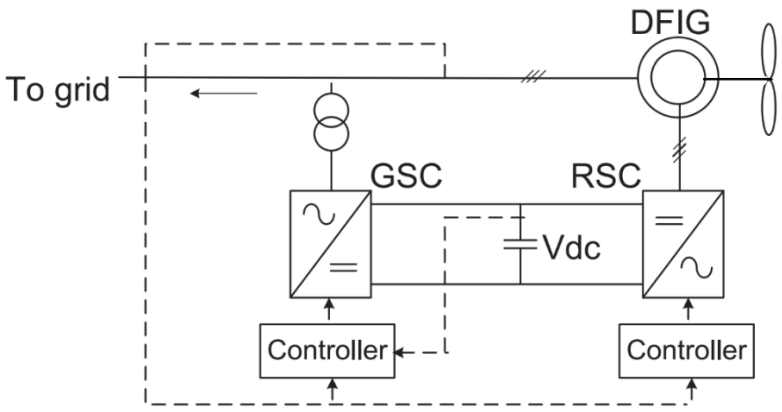

Figure 4.6 DFIG-based WECS.

The steady state equivalent circuit of the DFIG, referred to as a stator, is shown in Figure 4.7 below.

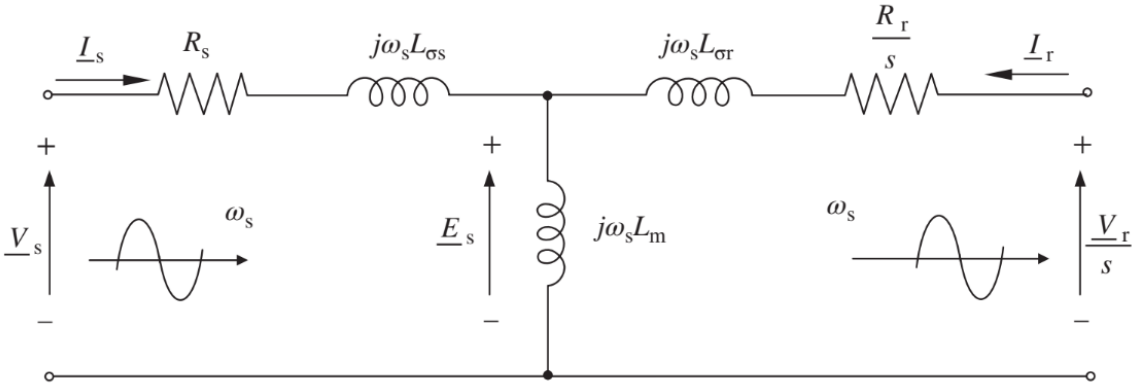

Figure 4.7 Steady-state equivalent circuit of DFIG referred to stator [67]. .

Where: I_s stator current, R_s stator resistance, J moment of inertia, w_s stator electrical angular speed, S slip, V_s stator voltage, V_r rotor voltage, I_r rotor current, L_m magnetizing inductance

The steady state parameters for DFIG machine are shown in table 4.2.

Table 4.4 DFIG steady state parameters

Parameter	**Value**	**Unit**
Stator frequency	50	hz
Mechanical power	1.5	MW
Rotational speed	1500	Rev/min
Stator voltage	690	V_s
Stator current	1760	Ampers (A)
Pair of poles	2	P
Rotor voltage	2070	V_r
Stator resistance	2.6×10^{-3}	Ohms (Ω)

Leakage inductance (Lsi)	0.087×10^{-3}	Henry (H)
Magnatizing inductance (L_m)	2.5×10^{-3}	H
Rotor resistance (R_r)	2.9×10^{-3}	Ω
Stator inductance (L_s)	2.587×10^{-3}	H
dc-link voltage	1150	v
dc-link capacitor	10000×10^{-6}	Farads (F)
Nominal power	$\frac{1.5}{0.9}$	(MW)

The rotor and stator turns ratios are indicated in the following equations:

$$\mu = \frac{N_s}{N_r} \quad \textbf{(4.6)}$$

$$E_{rs} = S\frac{E_s}{\mu} \quad \textbf{(4.7)}$$

The equations below can illustrate the power flow of a DFIG:

$$P_m = P_s + P_r P_{cus} - P_{cur} \quad \textbf{(4.8)}$$

$$P_{cus} = 3R_s(I_s)^2 \quad \textbf{(4.9)}$$

$$P_{cur} = 3R_r(I_r)^2 \quad \textbf{(4.10)}$$

Where: P_m is mechanical power, P_{cus} stator copper losses, and P_{cur} rotor copper losses.

The equations below demonstrate the machine's efficiency (η):

$$\eta = \frac{P_m}{P_s + P_r} \quad \textbf{(4.11)}$$

Where:

$$P_s = 3R_s(I_s)^2 + 3w_s L_m I_m I_s I_r^* \quad \textbf{(4.12)}$$

$$Q_s = 3w_s L_s(I_s)^2 + 3w_s L_m Re I_r I_s^* \quad \textbf{(4.14)}$$

$$P_r = 3R_r(I_r)^2 - 3Sw_s L_m I_m I_s I_r^* \quad \textbf{(4.13)}$$

$$Q_r = 3Sw_s L_r(I_r)^2 + 3Sw_s L_m Re I_s I_r^* \quad \textbf{(4.14)}$$

Where: P_s is stator active power, P_r rotor active power, Q_s stator reactive power, Q_r rotor reactive power, and I_m magnetizing current.

The electromagnetic torque can be calculated using:

$$P_{mec} = T_{em}\Omega_m = T_{em}\frac{W_m}{P} \quad \textbf{(4.15)}$$

$$T_{em} = 3PL_m IMI_r^* I_s \quad \textbf{(4.16)}$$

$$= 3\frac{L_m}{\sigma L_r L_s} PIM\emptyset_r \Phi_s \quad \textbf{(4.17)}$$

When one ignores stator and rotor copper losses, total power supplied to the grid is:

$$P_g = P_s + P_r \quad \textbf{(4.18)}$$

As shown in Figure 4.8, the RSC is attained inside a revolving d-q axis frame with the d-axis aligned with the position of the stationary winding flux vector.

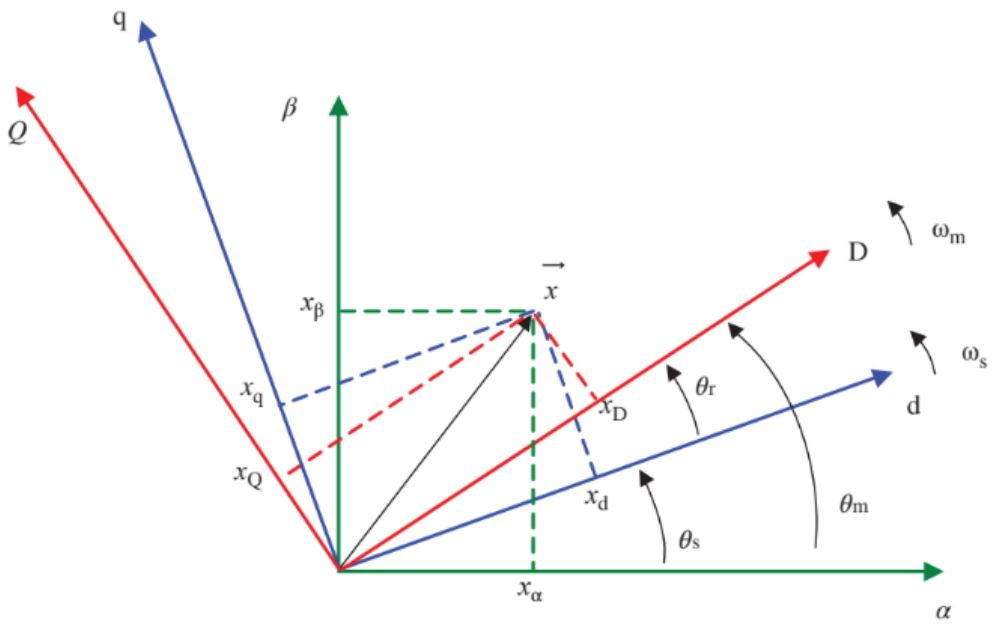

Figure 4.8 Three rotating reference frame that are not identical.

A space vector can be indicated in any of these frames by using inversion and direct rotational change. As a result, using Space Vector theory, the stator and rotor's three coils may be represented by two stationary coils for the stator and two rotating coils for the rotor. This includes the voltage equations listed below:

$$V_s = R_s i_s + \frac{d\Phi_s}{dt} \quad \textbf{(4.19)}$$

$$V_r = R_r i_r + \frac{d\Phi_r}{dt} \quad \textbf{(4.20)}$$

Where $\boldsymbol{P = \frac{d}{dt}}$ is the derivative operator, Φ_s stator flux, and Φ_r rotor flux.

If the equations above are written in a stationary reference frame, the rotor and stator equations can be provided as illustrated below:

$$V_{\alpha s} = R_s i_{\alpha s} + \frac{d\Phi_{\alpha s}}{dt} \quad \textbf{(4.21)}$$

$$V_{\beta s} = R_s i_{\beta s} + \frac{d\Phi_{\beta s}}{dt} \quad \textbf{(4.22)}$$

$$V_{\alpha r} = R_r i_{\alpha r} + \frac{d\Phi_{\alpha r}}{dt} \quad \textbf{(4.23)}$$

$$V_{\beta r} = R_r i_{\beta r} + \frac{d\Phi_{\beta r}}{dt} \quad \textbf{(4.24)}$$

In a space vector fixed reference frame, stator and rotor flow equations can be derived similarly to voltage equations.

$$\Phi_s = L_s i_s + L_m i_r \quad \textbf{(4.25)}$$

$$\Phi_{\beta s} = L_{\beta s} i_{\beta s} + L_\beta i_{\beta s} \quad \textbf{(4.26)}$$

$$\Phi_{\propto s} = L_{\propto s} i_{\propto s} + L_m i_{\propto s} \quad \textbf{(4.27)}$$

$$\Phi_r = L_m i_s + L_r i_r \quad \textbf{(4.28)}$$

$$\Phi_{\propto r} = L_m i_{\propto r} + L_r i_{\propto r} \quad \textbf{(4.29)}$$

$$\Phi_{\beta r} = L_m i_{\beta s} + L_r i_{\beta r} \quad \textbf{(4.30)}$$

As a result of the above-mentioned equations, the equivalent circuit of α is depicted in Figure 4.9, while the equivalent circuit of β is depicted in Figure 4.10.

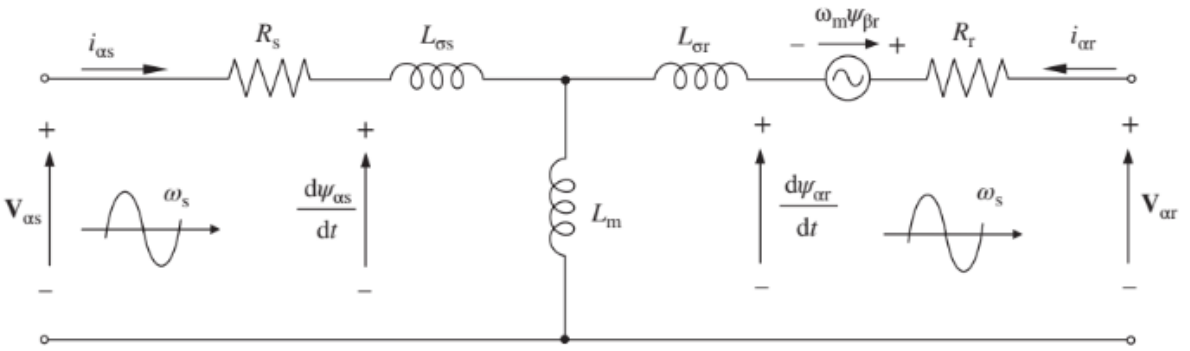

*Figure 4.9 Model of DFIG in the **α reference frame.***

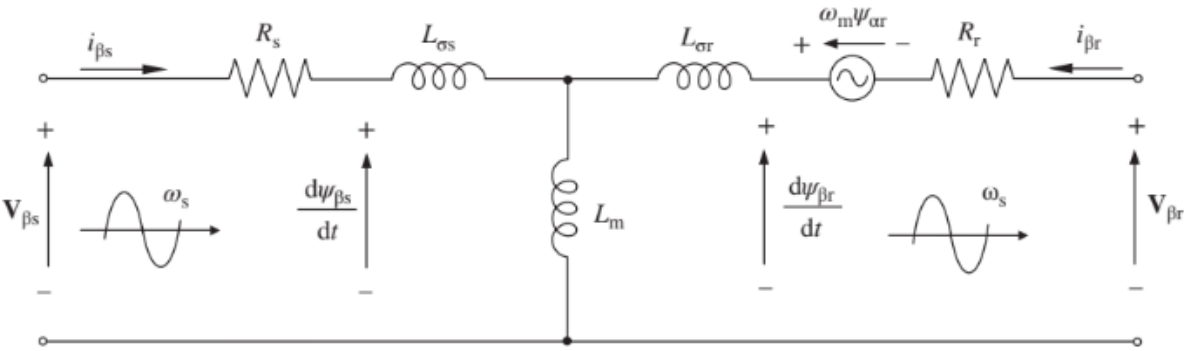

Figure 4.10 Model of DFIG in the β reference frame.

The following equations can be used to compute active and reactive power:

$$P_s = \frac{3}{2}\left(V_{\propto s} i_{\propto s} + V_{\beta s} i_{\beta s}\right) \quad \textbf{(4.31)}$$

$$P_r = \frac{3}{2}\left(V_{\propto r} i_r + V_{\beta r} i_{\beta r}\right) \quad \textbf{(4.32)}$$

$$Q_s = \frac{3}{2}\left(V_{\beta s} i_{\alpha s} - V_{\alpha s} i_{\beta s}\right) \quad \textbf{(4.33)}$$

$$Q_r = \frac{3}{2}\left(V_{\beta r} i_{\alpha r} + V_{\alpha r} i_{\beta r}\right) \quad \textbf{(4.34)}$$

The electromagnetic torque produced by a Doubly Fed Induction Generator is determined by the formulae below:

$$T_{em} = \frac{3}{2} P\left(\Phi_{\beta r} i_{\propto r} - \Phi_{\propto r} i_{\beta r}\right) \quad \textbf{(4.35)}$$

$$T_{em} = \frac{3}{2} L_m PLm(i_s i_r) \quad \textbf{(4.36)}$$

In addition, gain $\sigma = 1 - \frac{{L_m}^2}{L_s L_r}$ **(4.37)**

The following expression represents electromagnetic torque in conjunction with the mechanical motion equation, which demonstrates rotor speed performance:

$$T_e = \frac{3pL_m}{2}\left(i_{qs}.i_{dr} - i_{ds}.i_{qr}\right) \quad (4.38)$$

Where P is giving number of poles.

In terms of d-q voltage equations, the following space vector model is represented in a synchronous rotating frame:

$$V_{ds} = R_s i_{ds} + \frac{d\Phi_{ds}}{dt} - \omega_s \Phi_{qs} \quad \textbf{(4.39)}$$

$$V_{qs} = R_s i_{qs} + \frac{d\Phi_{qs}}{dt} + \omega_s \Phi_{ds} \quad \textbf{(4.40)}$$

$$V_{dr} = R_r i_{dr} + \frac{d\Phi_{dr}}{dt} - \omega_r \Phi_{qr} \quad \textbf{(4.41)}$$

$$V_{qr} = R_r i_{qr} + \frac{d\Phi_{qr}}{dt} + \omega_r \Phi_{dr} \quad \textbf{(4.42)}$$

The mathematical model represents stator and rotor flux in terms of decoupled currents:

$$\Phi_{ds} = L_s i_{ds} + L_m i_{dr} \quad \textbf{(4.43)}$$

$$\Phi_{qs} = L_s i_{qs} + L_m i_{qr} \quad \textbf{(4.44)}$$

$$\Phi_{dr} = L_m i_{ds} + L_r i_{dr} \quad \textbf{(4.45)}$$

$$\Phi_{qr} = L_m i_{qs} + L_r i_{qr} \quad \textbf{(4.46)}$$

The above equations were used to generate the corresponding electric circuit diagrams shown in Figures 4.11 and 4.12 below:

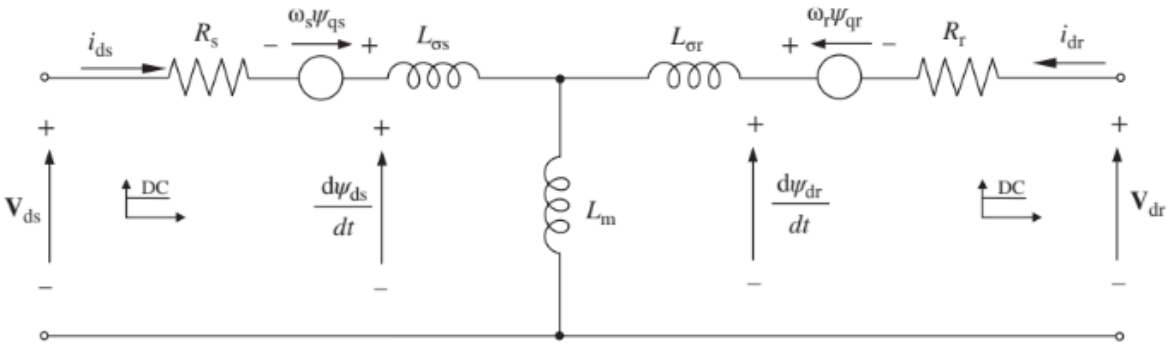

Figure 4.11 Circuital mode of DFIG in d-axis reference frame.

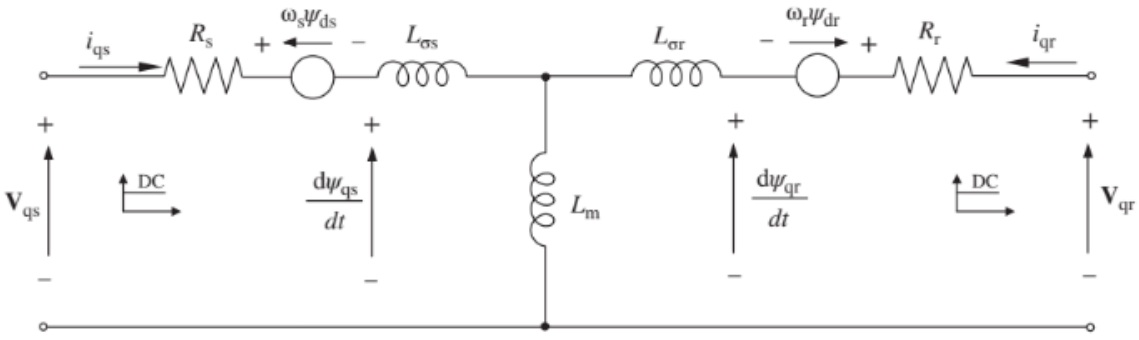

Figure 4.12 Circuital model of DFIG in q-axis reference frame.

Rotor voltages and stator voltages can be estimated as functions of rotor currents and stator currents, as shown below:

$$V_{dr} = R_r i_{dr} + \sigma L_r \frac{d}{dt} i_{dr} - W_r \sigma L_r i_{qr} + \frac{L_m}{L_s} \Phi_s \quad \textbf{(4.46)}$$

$$V_{qr} = R_r i_{qr} + \sigma L_r \frac{d}{dt} i_{qr} + W_r \sigma L_r i_{dr} + W_r \frac{L_m}{L_s} \Phi_s \quad \textbf{(4.47)}$$

4.2.4. Control strategy for a grid-connected DFIG-based WECS

a. Rotor-Side Converter Control System

Figure 4.6 depicts the entire DFIG-based WECS. This section only exhibits the RSC controller topology. The induction machine rotor is excited by the rotor-side converter (RSC). This PWM converter allows one to manage the torque, and thus the speed of the DFIG, as well as the power factor at the stator terminals. Depending on the wind speed, the rotor-side converter provides a variable excitation frequency. In one popular approach, the induction machine is controlled by a synchronously rotating dq-

axis frame, with the d-axis oriented along the stator-flux vector position. This is called stator-flux orientation (SFO) vector control. This results in a decoupling of the electrical torque and rotor excitation current. As a result, active and reactive power are managed independently of one another. The rotor-side converter's control scheme is organized in a generic manner, with two sets of two controllers. A schematic block diagram for the rotor-side converter control is shown in Figure 4.13 below. The reference q-axis rotor current I_{qr} can be calculated using either an outside speed control loop or machine-imposed reference torque. One outside controller is responsible for controlling the speed error signal in terms of maximum power point tracking in speed-control mode. An additional controller is also necessary to produce the reference current for the direct axis rotor current loop circuit, and active power is controlled by controlling the q-axis rotor current. I_{dr} and I_{qr} are error signals processed by the controllers connected to them to make V_{rd} and V_{rq}, respectively.

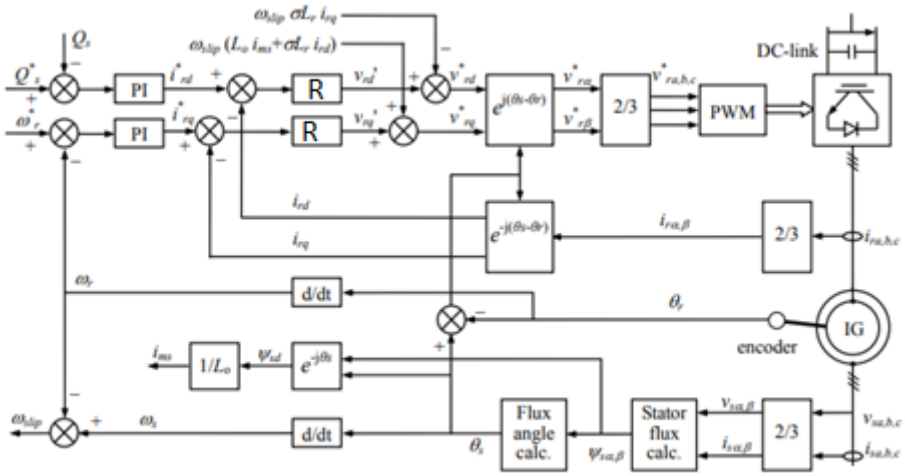

Figure 4.13 DFIG rotor side converter control system.

b. Grid-Side Converter Control System

Figure 4.6 depicts the entire DFIG-based WECS. This section only exhibits the GSC controller topology. The grid-side converter is used to modify the capacitor voltage as well as the d-axis and q-axis currents. The GSC control structure shown in Figure 4.14 below contains an outside loop for adjusting the DC-link voltage. Through the grid interface inductance, the grid-side converter controls the flow of real and reactive power to the grid. A reference frame oriented along the stator voltage vector position

is also used, allowing independent control of the active and reactive power flowing between the grid and the converter, where $V_{\alpha g}$ and $V_{\beta g}$ are grid-side voltage stationary frame components of the converter. The reference frame's d-axis is parallel to the grid voltage angular position. Since the voltage amplitude is constant, V_{gq} is zero and V_{gd} is constant. The quadratic component I_q of the grid current is utilized to regulate the flow of reactive power. The direct current component of the converter side I_d is used to control the active power. The difference between the DC-side reference and measured voltages ($V_{dref} - V_{dc}$) serves as the DC voltage input to the controller. The regulator output generates the reference for the direct component of the source current, I_{dref}.

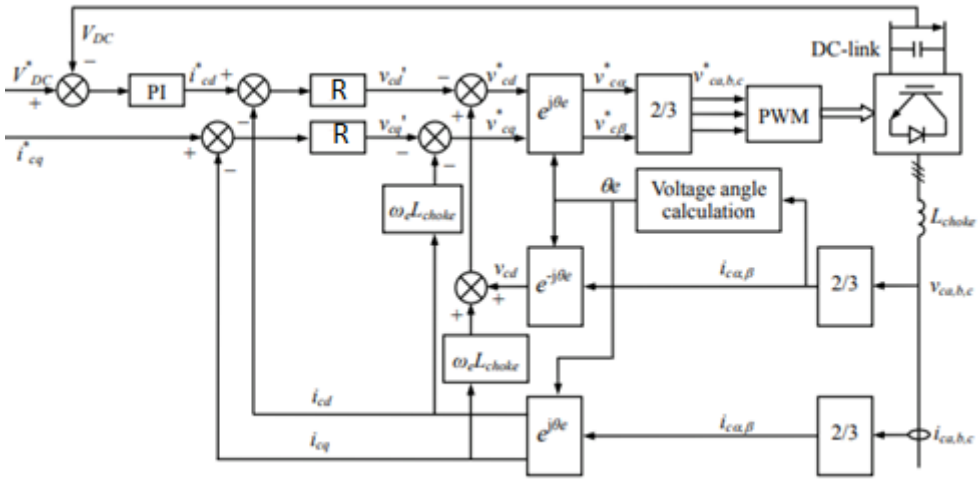

Figure 4.14 DFIG grid side converter control system.

4.2.5. PMSG-based wind energy conversion system

As seen in Figure 4.15, the PMSG machine has a three-phase stator and rotor.

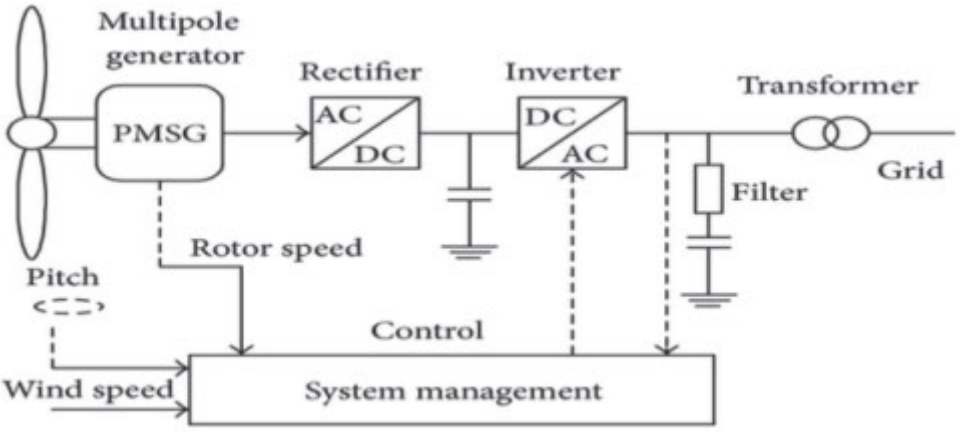

Figure 4.15 Block diagram of wecs incorporating PMSG.

The d-axis and q-axis circuit diagrams illustrated in Figure 4.16 can be used to develop the dynamic voltage equation of the PMSG. A constant magnitude equivalent current source (I_f) is used to represent the permanent magnet. Table 4.5 displays the PMSG steady state parameters.

Table 4.5 PMSG parameters.

Parameter	Value	unity
Rated power	1.5	MW
Pole pairs	40	p
Stator resistance	3.17×10^{-3}	Ω
Stator inductance	3.07×10^{-3}	H
Moment of inertia (J)	10000	$k.m^2$
DC-link voltage	1150	v
Capacitor of the dc-link	0.023	F

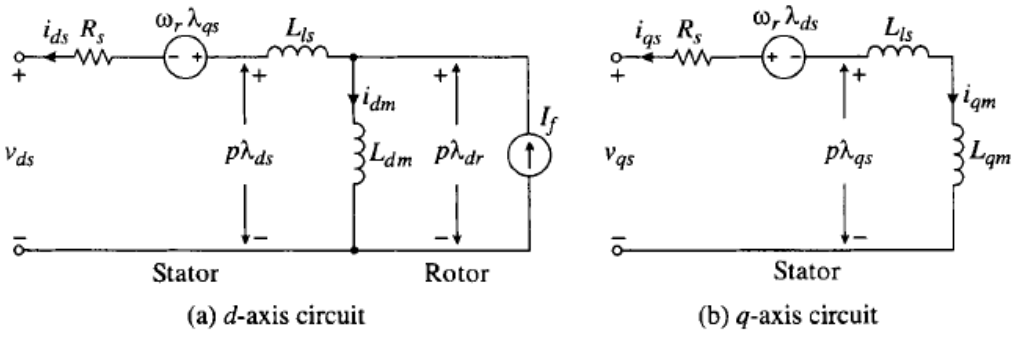

Figure 4.16 General d-q axis model of PMSG.

The PMSG's dynamic voltage equations can be represented in d-q co-ordinates using the following equations:

$$\lambda_{ds} = -L_{ls} i_{ds} + L_{dm}(I_f - i_{ds}) = -(L_{ls} + L_{dm}) i_{ds} + L_{dm} I_f = -L_d i_{ds} + \lambda_r \quad \textbf{(4.48)}$$

$$\lambda_{qs} = -(L_{ls} + L_{qm}) i_{qs} = -L_q i_{qs} \quad \textbf{(4.493)}$$

$$v_{ds} = -R_s i_{ds} - w_r \lambda_{qs} + p\lambda_{ds} \quad \textbf{(4.50)}$$

$$v_{qs} = -R_s i_{qs} + w_r \lambda_{ds} + p\lambda_{qs} \quad \textbf{(4.51)}$$

Where:

$$\lambda_r = L_{dm} i_f \quad \textbf{(4.52)}$$

$$L_d = L_{ls} + L_{dm} \quad \textbf{(4.53)}$$

$$L_q = L_{ls} + L_{qm} \quad \textbf{(4.54)}$$

$$v_{ds} = -R_s i_{ds} + w_r L_q i_{qs} - L_d p i_{ds} \quad \textbf{(4.55)}$$

$$v_{qs} = -R_s i_{qs} - w_r L_d i_{ds} + w_r \lambda_r - L_q p i_{qs} \quad \textbf{(4.56)}$$

Figure 4.17 depicts a simplified model for PMSG obtained from equations 4.62 and 4.63.

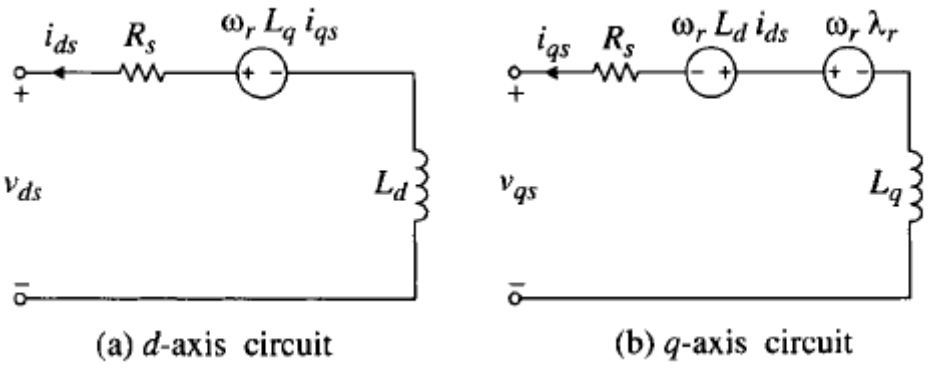

Figure 4.17 Simplified model for PMSG.

The PMSG's mechanical dynamics are represented as follows:

$$J\frac{d\omega_r}{dt} + D\omega_r = T_m - T_e \quad \textbf{(4.57)}$$

The electromagnetic torque T_e can be calculated as follows:

$$T_e = \frac{3p}{2}[\lambda_r i_{qs} - (L_d - L_q) i_{ds} iqs] \quad \textbf{(4.58)}$$

The true power (P) and reactive power (Q) of the PMSG are expressed into d-q coordinates as follows:

$$P = \frac{3}{2}\left[v_{sd} i_{sd} + v_{sq} i_{sq}\right] \quad \textbf{(4.59)}$$

$$Q = \frac{3}{2}\left[v_{sq} i_{sd} - v_{sd} i_{sq}\right] \quad \textbf{(3.60)}$$

4.2.6. Control strategy for a grid-connected PMSG-based WECS

Figure 4.15 depicts the entire DFIG-based WECS. This section only exhibits the GSC controller topology. The PMSG wind turbine generator's energy storage mechanism was employed to improve fault-ride-through capability. This machine comprises a bi-directional buck-boost converter and an ultra-capacitor that is connected in parallel to the converter's DC-link. To maximum operation, the PMSG stator is connected to the

power supply via a back-to-back converter that uses a vector control approach. Figure 4.18 shows the GSC control structure. The DC-link voltage is controlled by an outside loop. Through the grid interface inductance, the grid-side converter controls the flow of real and reactive power to the grid. A reference frame oriented along the stator voltage vector position is also used, allowing independent control of the active and reactive power flowing between the grid and the converter. Where $V_{\alpha g}$ and $V_{\beta g}$ are grid-side voltage stationary frame components of the converter, the reference frame's d-axis is parallel to the grid voltage angular position. Since the voltage amplitude is constant, V_{gq} is zero and V_{gd} is constant. The quadratic component I_q of the grid current is utilized to regulate the flow of reactive power. The converter side's Id current is used to regulate the active power. The difference between the DC-side reference and measured voltages ($V_{dref} - V_{dc}$) serves as the DC voltage input to the controller. The regulator output generates the reference for the direct component of the source current, I_{dref}. The PMSG generator side control system is replaced by the diode rectifier.

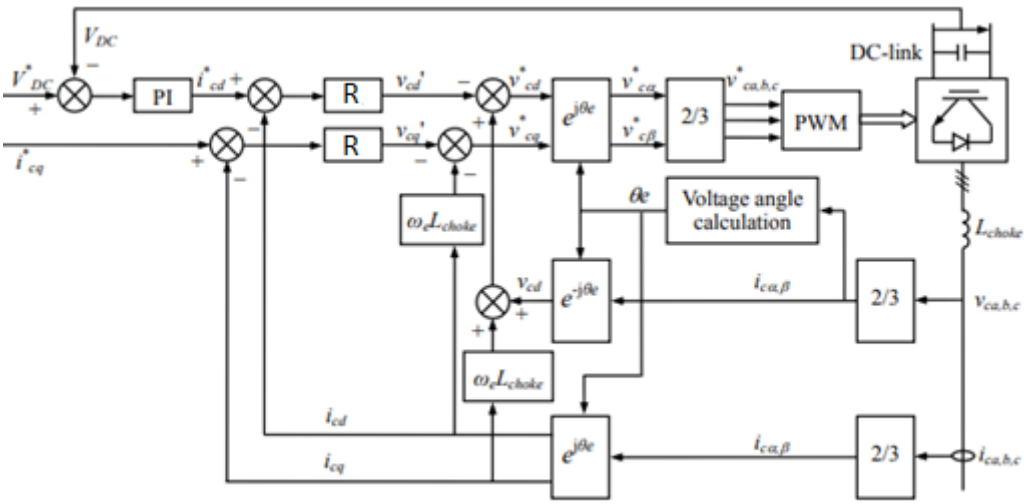

Figure 4.18 PMSG grid side converter control system.

4.2.7. Analysis of Fuzzy Controller, PID Controller, and Fuzzy-PID Controller

a. FUZZY Logic Controller

The fuzzy logic controller is a type of non-linear conventional controller that consists of three phases: fuzzification, fuzzy rule basis, and defuzzification. Figure 4.19 illustrates the structure of the fuzzy logic controller employed in this study. Fuzzification is the process of transforming the controller's crisp input values into fuzzy input values[68]. A fuzzy variable's value is defined by a linguistic phrase such as "large," "small", "high", "low" or "medium", each of which is specified by a unique membership function. The fuzzy rule base encapsulates the rules that connect the inputs and outputs, whereas defuzzification converts the produced fuzzy value to a numeric value. The fuzzy logic controller receives two input signals: the error signal e (t) and the rate of change of the error signal $e^{\cdot}(t)$. Separately, the rotor current components I_{dr} and I_{qr} are fuzzified using an eleven-input fuzzy set via two FLCs. In Figure 4.20, the corresponding membership functions for the inputs e (t) and u (t) are shown.

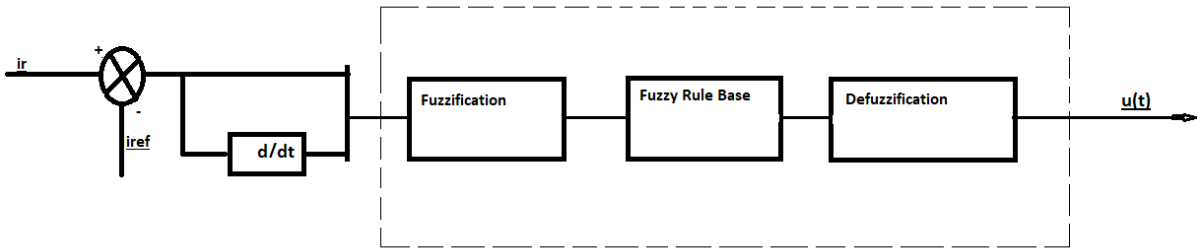

Figure 4.19 Fuzzy-logic structure.

Inputs 1 and 2 represent the error signal e(t) and the rate of change of the error signal $e^{\cdot}(t)$. The membership function for all of the previously specified parameters has been set to a triangular-shape membership function (T_{rimf}). The membership function has a range of -1 to 1. Each of the fuzzy input and output subsets ranges from negative very large (NV) to positive very large (PV). To build a collection of eleven membership functions for each fuzzy variable, each subset is associated with a triangle membership function. NV, NL, NB, NM, NS, ZR, PS, PM, PB, PL, PV are linguistic variables that stand for negative very large, negative large, negative big, negative medium, negative small, zero, positive small, positive medium, positive big, positive huge, and positive very large. $e^{\cdot}(t)$ has the equivalent membership functions as e (t).

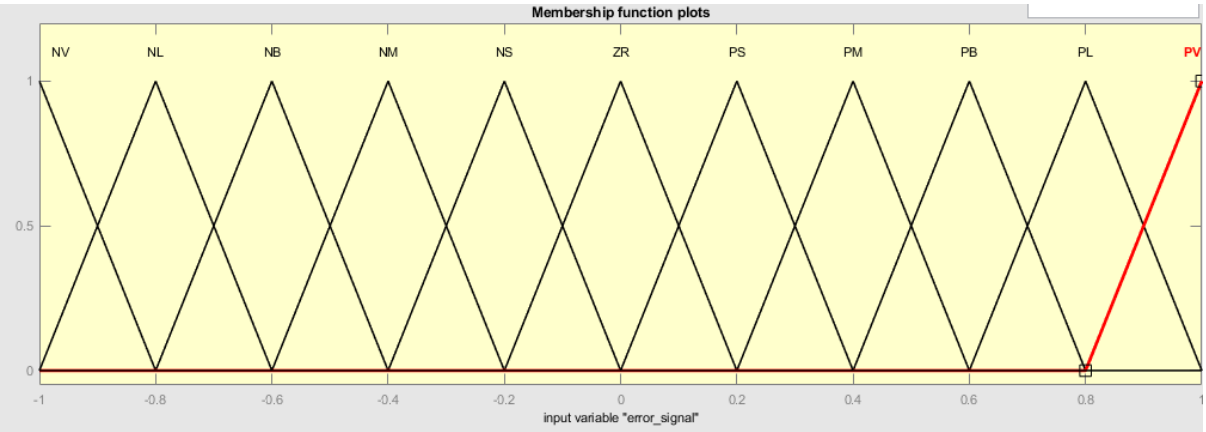

Figure 4.20 Membership functions.

The control rules are written in such a way that for each combination of e (t) and $e^{\cdot}(t)$, a fuzzy set of control inputs is assigned. The rule base is summarized in Table 4.3.

Table 4.6 Membership functions.

e(t) / $e^{\cdot}(t)$	NV	NL	NB	NM	NS	ZR	PS	PM	PB	PL	PV
NV	NV	NV	NL	NB	NB	NM	NM	NS	NS	ZR	ZR
NL	NV	NL	NL	NB	NB	NM	NM	NS	NS	ZR	ZR
NB	NL	NL	NB	NB	NM	NM	NS	NS	ZR	ZR	PS
NM	NL	NB	NB	NM	NM	NS	NS	ZR	ZR	PS	PS
NS	NB	NB	NM	NM	NS	NS	ZR	ZR	PS	PS	PM
ZR	NB	NM	NM	NS	NS	ZR	ZR	PS	PS	PM	PM
PS	NM	NM	NS	NS	ZR	ZR	PS	PS	PM	PM	PB
PM	NM	NS	NS	ZR	ZR	PS	PS	PM	PM	PB	PB
PB	NS	NS	ZR	ZR	PS	PS	PM	PM	PB	PB	PL
PL	NS	ZR	ZR	PS	PS	PM	PM	PB	PB	PL	PL
PV	ZR	ZR	PS	PS	PM	PM	PB	PB	PL	PL	PV

The columns denote the error e (t), whereas the rows denote the rate of change of the error $e^{\cdot}(t)$. Each pair denotes the output level associated with u. (t).

b. PID CONTROLLER

The PI controller was created in Simulink by utilizing a built-in PID controller block. In this research, PID controller regulates the I_q and I_d currents in grid-side and rotor-side controllers. Figure 4.21 depicts the circuit diagram for a FUZZY-PID controller. In addition, this control topology provides a robust fault response and a steady-state robust control system for the DFIG-based WECS.

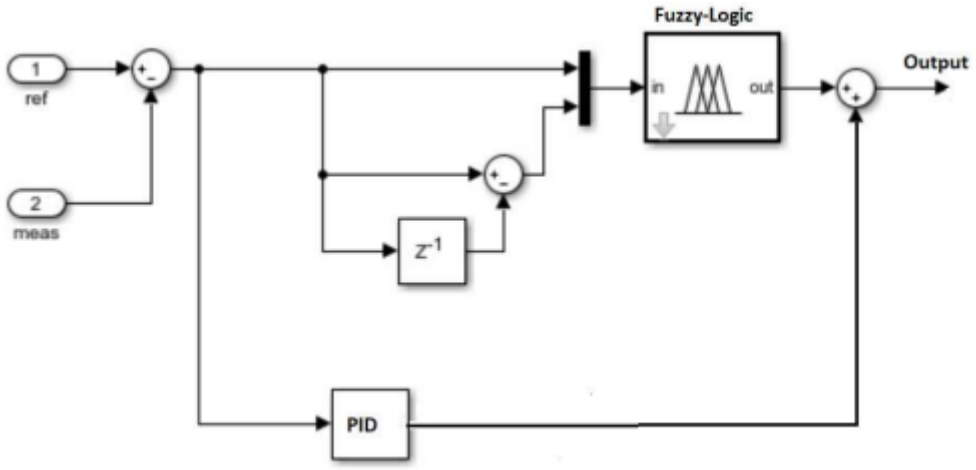

Figure 4.21 Fuzzy-PID controller.

The error signal generated by the proposed controllers is displayed as follows:

For rotor side converter control

$$e(t)_{(d,q)} = i_{r(d,q)} - i_{r(d,q)ref} \quad \textbf{(4.61)}$$

For grid side converter control

$$e(t)_{(d,q)} = i_{g(d,q)} - i_{g(d,q)ref} \quad \textbf{(4.62)}$$

The PI and PID controllers' coefficients are tuned by a trial-and-error tuning procedure to ensure rapid reaction at various wind speed values and maximum power extraction. When the gains for both the grid and rotor side controllers are as shown in Table 4.4 below, the system is at its best.

Table 4.7 PI and PID parameters.

	PI and PID Parameters		
Regulators	Kp	Ki	Kd
Grid-side-currents	0.85	4.95	0.025
Rotor-side-currents	0.58	7.95	0.025
DC-Bus	7.85	390	0
Speed-control	3.5	0.65	0
Pitch-Angle	3.2	30.5	0

4.3. Summary

This chapter has achieved the modelling and simulation of the wind energy conversion system incorporating a doubly fed induction generator or a permanent magnet synchronous generator. In this chapter, the analysis of control strategies was based on matching the active power, reactive power, and dc-link voltage to their nominal values. From the modelling and simulation results, it is seen that of the different control strategies, the Fuzzy-PID control strategy appears to outperform the other strategies (including Fuzzy-logic controller and PID controller). The results obtained from MATLAB/SIMULINK software for these control strategies are analysed and discussed in chapter 5.

CHAPTER 5:

RESULT ANALYSIS AND DISCUSSION

5.1. Introduction

This chapter provides a dynamic performance analysis of the control strategy, which is the DFIG-based WECS integrating a VSC with a Fuzzy-PID controller connected to a grid. The control strategy is further compared to the DFIG-based WECS with a PID controller connected to a grid, the PMSG-based WECS with a PID controller connected to a grid, and the DFIG-based WECS with a Fuzzy logic controller.

5.2. Dynamic performance of a DFIG-based WECS integrating a VSC with a fuzzy-PID controller connected to a grid

Figure 5.1 below shows how the active power of a DFIG-based WECS with a Fuzzy-PID controller responds to a single phase-ground fault on the power system.

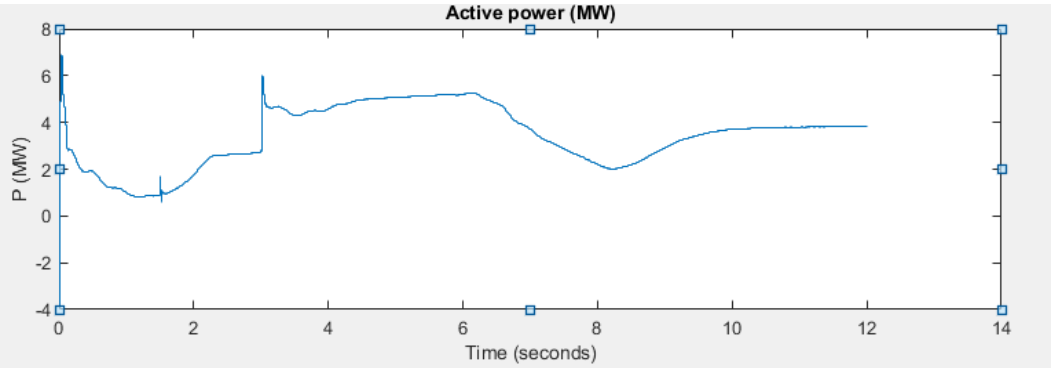

Figure 5.1 Active power of DFIG-based WECS with Fuzzy-PID.

Figure 5.2 shows what happens to the DC-link voltage of a DFIG-based WECS with a Fuzzy-PID control when a single phase to ground fault occurs on the power system.

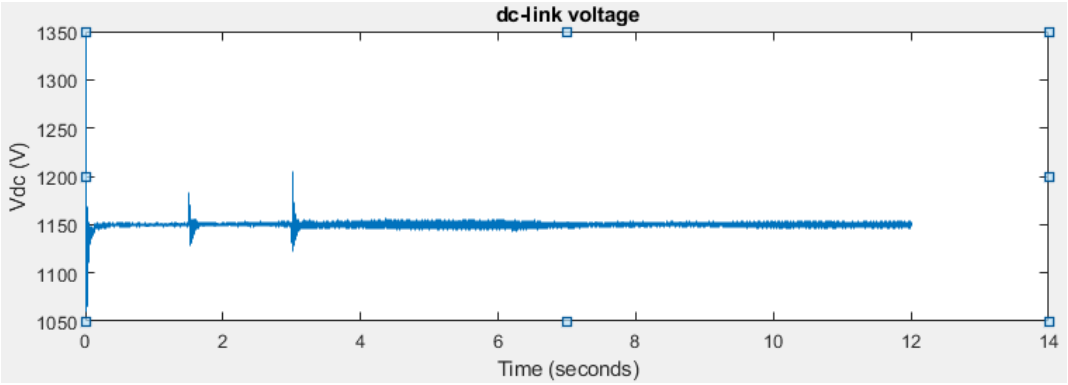

Figure 5.2 DC-link voltage of DFIG-based WECS with Fuzzy-PID.

Figure 5.3 shows that the DFIG-based Fuzzy-PID controller was able to support the grid by injecting reactive current when there was a single phase-ground fault in the power system.

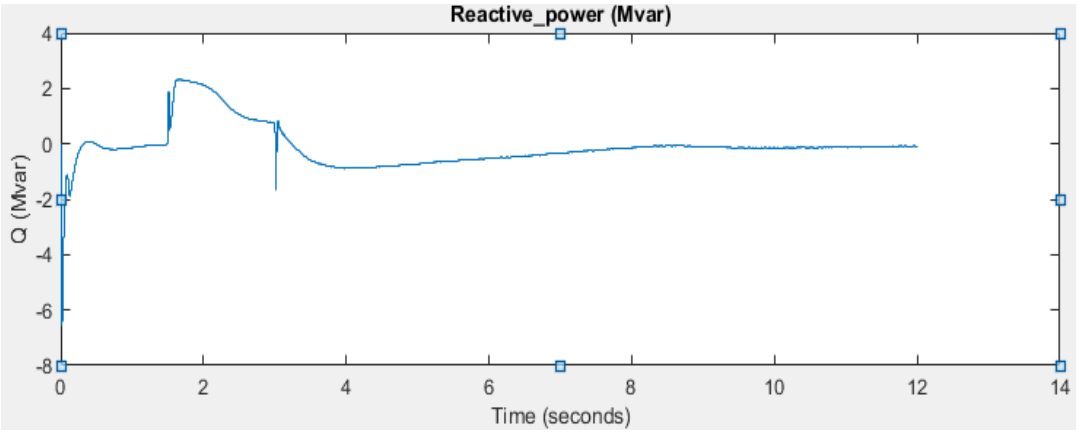

Figure 5.3 Reactive power of DFIG-based WECS with Fuzzy-PID.

5.3. Dynamic performance of a DFIG-based WECS with a PID controller connected to a grid

Figure 5.4 depicts how the active power of a DFIG-based WECS with a PID controller reacts to a single phase-ground fault on the power system.

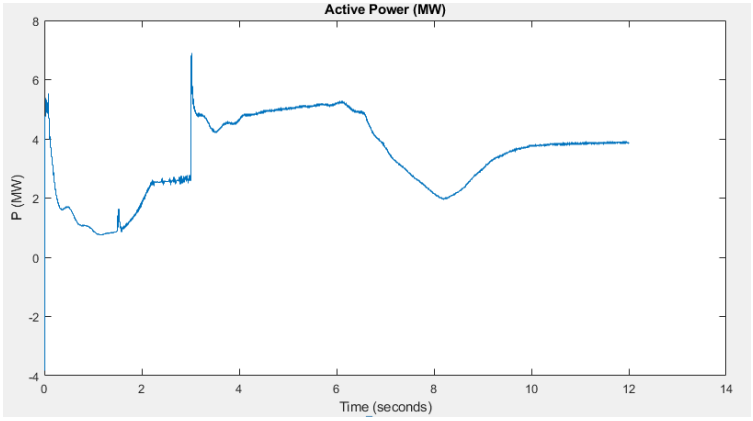

Figure 5.4 Active power of a DFIG-based WECS with a PID controller.

Figure 5.5 below depicts what occurs to the DC-link voltage of a DFIG-based WECS with PID control when the power system has a single phase to ground fault.

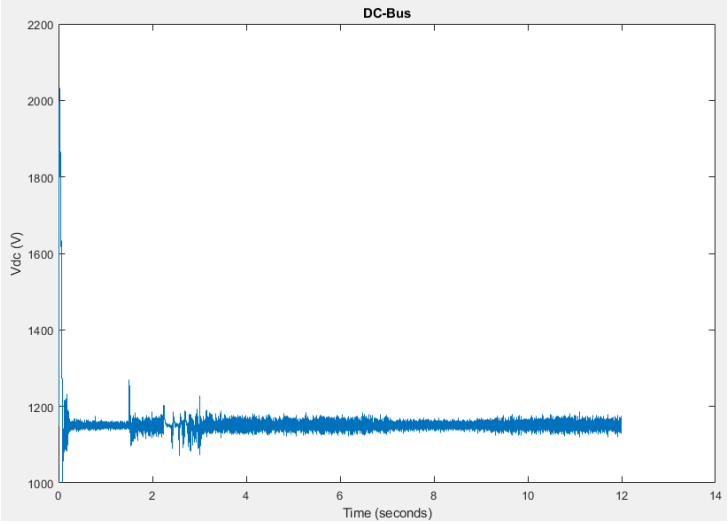

Figure 5.5 DC-link voltage of a DFIG-based WECS with a PID controller.

Figure 5.6 demonstrates that the DFIG-based WECS with a PID controller was able to support the grid during a power system disturbance by injecting reactive current. However, the reactive power performance has numerous harmonics.

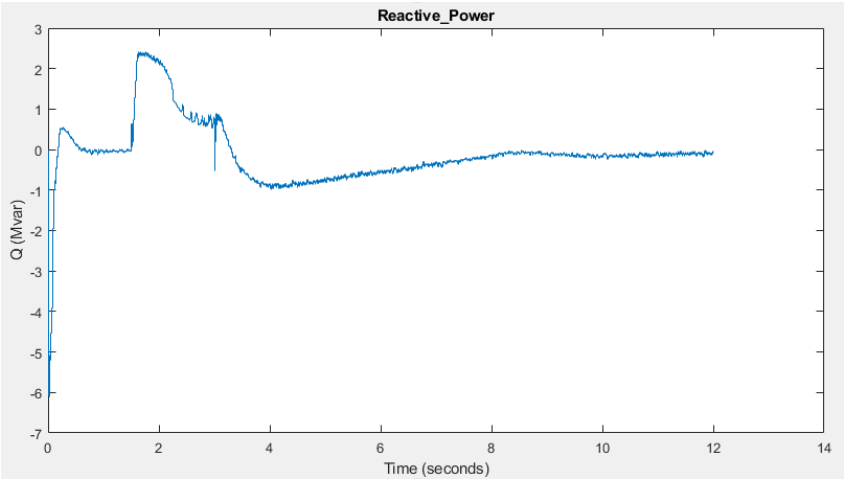

Figure 5.6 Reactive power of a DFIG-based WECS with a PID controller.

5.4. Dynamic performance of a PMSG-based WECS with a PID controller connected to a grid

Figure 5.7 below shows how a PMSG-based WECS with a PID controller responds to a single phase-ground fault on the power system in terms of active power.

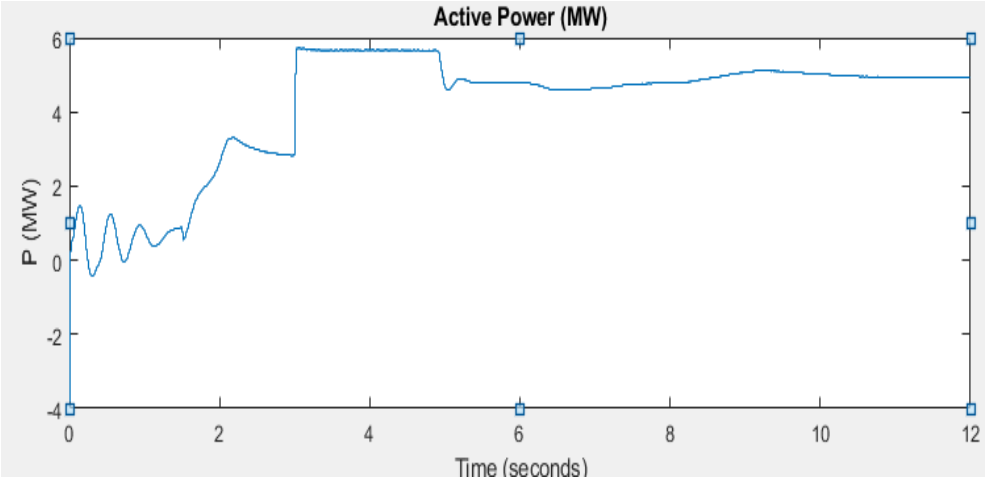

Figure 5.7 Active power of a PMSG-based WECS with a PID controller.

During a grid fault, the DC-link voltage of the PMSG-based WECS with a PID controller spikes to high values, as depicted in Figure 5.8.

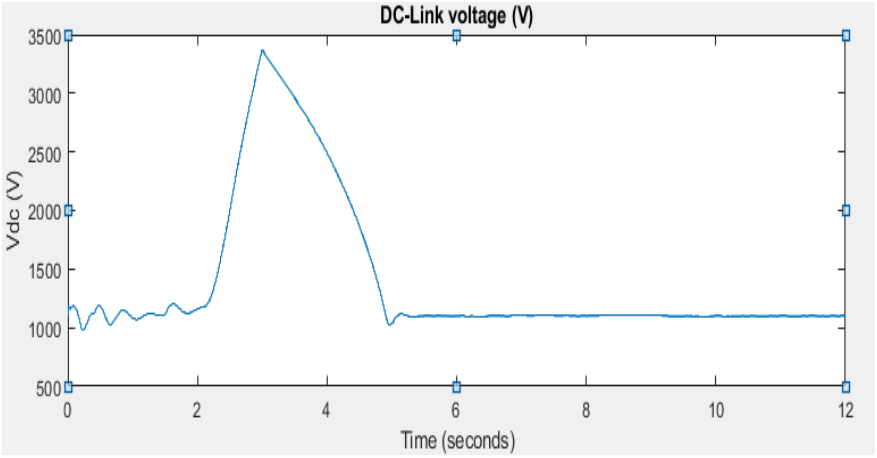

Figure 5.8 DC-link voltage of the PMSG-based WECS with a PID controller.

Figure 5.9 shows that the PMSG-based WECS with a PID controller was able to support the power system when there was a single phase-ground fault on the power system. This was done by injecting reactive power.

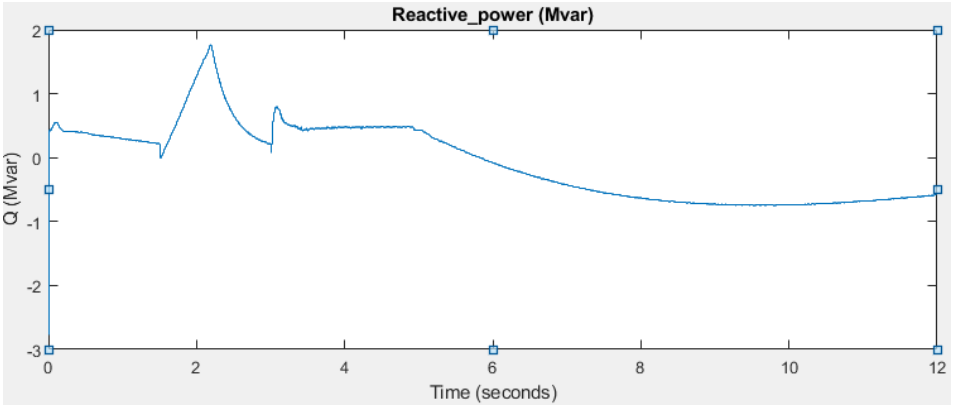

Figure 5.9 Reactive power of the PMSG-based WECS with a PID controller.

5.5. Dynamic performance of a DFIG-based WECS with a Fuzzy logic controller

The active power of a DFIG-based WECS with a Fuzzy logic controller is shown in Figure 5.10 in response to a single phase-ground fault.

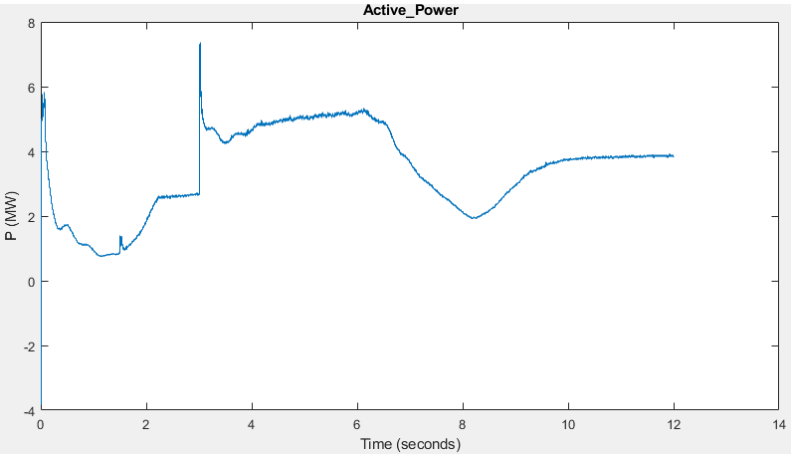

Figure 5.10 Active power of a DFIG-based WECS with a Fuzzy logic controller.

Figure 5.11 shows what occurs to the DC-link voltage of a DFIG-based WECS with fuzzy logic control when a single phase to ground fault occurs on the power system.

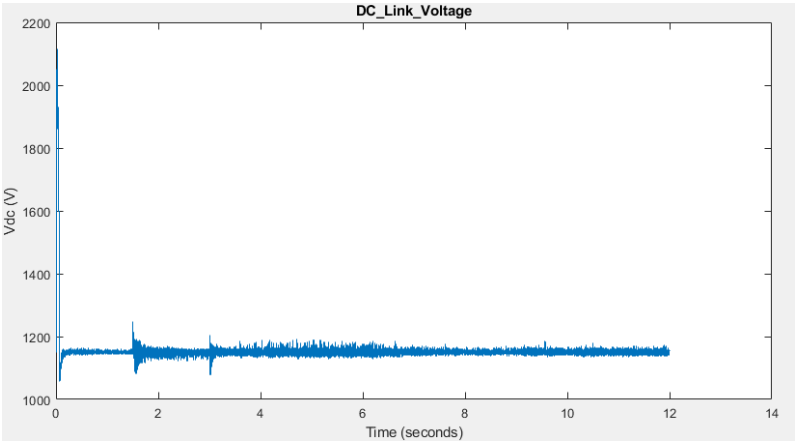

Figure 5.11 DC-link of a DFIG-based WECS with a Fuzzy logic controller.

Figure 5.12 below shows how the DFIG-based Fuzzy logic controller was able to support the grid by injecting reactive current when a single phase-ground fault occurred on the power system.

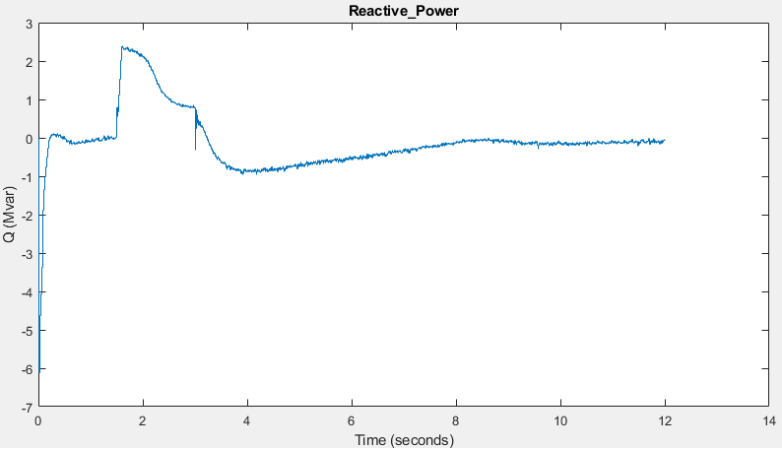

Figure 5.12 Reactive power of a DFIG-based WECS with a Fuzzy logic controller.

5.6. Comparative analysis with reference to the Fuzzy-logic controller

The comparison of performance for the different WECS with controller as compared to the WECS model incorporating a Fuzzy-PID controller is done in terms of the percentage overshoot and undershoot and the settling time of the voltage and current signals, as well as in term of fault ride through capability.

Table 5.1 provides the results of analysis of the DC-link voltage characteristic internal to the different WECS topologies and compared to thel DFIG-based WECS with a Fuzzy-PID controller when a fault actually occurs in the grid or power system. According to the table below, when there is a fault on the grid, the DFIG-based WECS with a Fuzzy-PID controller has more robust DC-Link voltage performance than other models.

Table 5.1 Comparison of the DC-link voltage.

WECS Models	**Amplitude of overshoot (Volt)**	**Amplitude of undershoot (Volt)**	**Settling times (s)**
DFIG-based WECS with a Fuzzy-PID controller connected to a grid.	1200	1125	2.5

DFIG-based WECS with a PID controller connected to a grid	1250	1100	2.6
PMSG-based WECS with a PID controller connected to a grid.	3400	1000	4.5
DFIG-based WECS with a Fuzzy-logic controller connected to a grid.	1240	1500	3

Table 5.2 below provide the results of the analysis of the reactive power output characteristic of the different WECS topologies and is compared with theDFIG-based WECS with a Fuzzy-PID controller during a power system disturbances. According to the table below, the DFIG based WECS incorporating Fuzzy-PID controller responds efficiently in terms of system support by injecting and absorbing reactive power. As a result, it offers superior fault-ride through capacity as compared to other models.

Table 5.2 Comparison of reactive power.

WECS Models	**Overshoot (Mvar)**	**Undershoot (Mvar)**	**Settling times (s)**
DFIG-based WECS with a Fuzzy-PID controller	2	-2	3.8

connected to a grid.			
DFIG-based WECS with a PID controller connected to a grid.	2.5	-1	8
PMSG-based WECS with a PID controller connected to a grid.	1.9	-0.9	6
DFIG-based WECS with a Fuzzy-logic controller connected to a grid.	2.5	-1	8

Table 5.3 provides the results of the analysis of the active power output characteristic of the different WECS topologies and is compared with theDFIG-based WECS with a Fuzzy-PID controller during a power system disturbance. The table below demonstrates that the proposed model took less time than other models to meet the predetermined value for active power. As a result, active power has a significant impact on power system frequency.

Table 5.3 Comparison of active power.

WECS Models	**Overshoot (MW)**	**Undershoot (MW)**	**Settling times (s)**
DFIG-based WECS with a Fuzzy-PID controller connected to grid.	6	1	3
DFIG-based WECS with a PID controller connected to a grid.	7	0.5	3.8
PMSG-based WECS with a PID controller connected to a grid.	5.9	-0.1	5
DFIG-based WECS with a Fuzzy-logic controller connected to a grid.	7.8	0.5	4.2

Table 5.4 below summarizes the overall result of comparison with reference tothe DFIG-based WECS integrating a VSC with a Fuzzy-PID controller connected to a grid.

Table 5.4 Comparison of WECS models.

WECS Models	DC-link voltage	Reactive power	Active power
DFIG-based WECS with a Fuzzy-PID controller connected to a grid.	It provides robust regulation of DC-link voltage during grid faults in terms of overshoot. Therefore, damage to the generator's rotor is avoided.	The model performs admirably when it comes to providing grid support during faults by injecting reactive power. Additionally, once the fault has been cleared, it can operate at about 0 Mvar, which is what the standard grid code requires.	The system's active power was greatly reduced during grid faults, but after the fault was cleared, the system resumed normal operation. As a result, active power has a significant impact on power system frequency.
DFIG-based WECS with a PID controller connected to a grid.	The DC-link voltage is marginally higher and oscillates significantly, which may result in machine malfunction.	During a grid fault, the model gives reactive assistance that oscillates, which may not be sufficient for a stable power system.	When a fault occurs, the model provides active power with oscillations to a power system. This may significantly impact the power system frequency.
PMSG-based WECS with a PID controller connected to a grid.	It provides a DC-link voltage nearly three times greater than the reference voltage. This could cause system damage. It also necessitates additional safeguards.	The model can provide reactive power support for the grid. However, it cannot operate at 0 Mvar once the fault has been cleared, as per standard grid code requirements.	In terms of active power supply, the model is more robust than the DFIG-based WECS incorporating Fuzzy-PID. The performance of DC-link voltage and reactive power, however, makes the DFIG-based WECS with Fuzzy-PID controller superior to the PMSG-based WECS with

			a PID controller model.
DFIG-based WECS with a Fuzzy-logic controller connected to a grid.	When compared to the DFIG-based WECS with a fuzzy-PID controller, it has a larger DC-link voltage overshoot.	The system has the capability of supplying reactive power to the grid. However, stabilizing the system or operating at 0 Mvar takes a lengthy time (8 seconds).	The model supplies the power system with unhealthy active power (power oscillations).

5.7. Summary

This section evaluated the suggested topology's dynamic performance analysis, which is the DFIG-based WECS that integrates a VSC with a Fuzzy-PID controller and is grid-connected. Further comparisons were made between the DFIG-based WECS with Fuzzy-PID controller and the DFIG-based WECS with a PID controller connected to a grid; the PMSG-based WECS with a PID controller connected to a grid; and the DFIG-based WECS with a fuzzy logic controller connected to a grid. As demonstrated by the experiment, the DFIG based WECS with a Fuzzy-PID controller exhibits superior performance in comparison to existing models.

CHAPTER 6:
CONCLUSION AND FUTURE WORK

6.1. Conclusion

The main objective of this study was to investigate the dynamic performance of a DFIG-based WECS incorporating a voltage source converter with a Fuzzy-PID controller connected to the grid. The purpose of this research was to examine South Africa's most critical technical grid code needs. Grid code requirements apply to all RDGs linked to the grid, regardless of their categorization, and handle both normal and fault operating situations at the point of connection. This thesis discussed the voltage and frequency operating conditions under fault and normal conditions. As a result, RDGs must inject and absorb reactive current as needed. To investigate these criteria, this thesis first compared the two fastest developing RDGs, DFIG and PMSG-based wind turbines. According to the data, DFIG is more effective than PMSG. Additionally, a 1.5 MW DFIG wind turbine controller employs PID, Fuzzy-PID, and Fuzzy logic architectures to boost the wind turbine's performance. Aerodynamic, mechanical, electrical and control system modelling of a DFIG-based wind turbine were accomplished. MATLAB and SIMULINK were used to create the model. The dynamic performance indicates that the Fuzzy-PID controller provides the optimum performance for enhancing the wind turbine's performance. Pitch angle, speed and DC-link voltage regulation may require additional time, as some of these controllers require historical performance data from the controlled plant. Fuzzy-pid control should be implemented not only in current-loops, but also in pitch angle control, DC-link control, and speed control in the future to increase system performance. It is also essential to apply optimization algorithms such as particle swarm optimization to improve PID algorithm tuning, such as how they are tuned.

6.2. Scope for future work

Optimization approaches can be utilized to eliminate oscillations in the DC-link voltage of the DFIG-based wind turbine, or to replace the PID controller with a Fuzzy-PID controller in future work. Additionally, to enhance system performance, Artificial Neuro Inference System, Fuzzy type-2, and interval type-2 Fuzzy logic control systems must be considered. Finally, a hybrid RDG comprising PMSG and DFIG should be considered for enhanced power system support.

REFERENCES

1. Panwar, N., S. Kaushik, and S. Kothari, *Role of renewable energy sources in environmental protection: A review.* Renewable and sustainable energy reviews, 2011. **15**(3): p. 1513-1524.
2. Bull, S.R., *Renewable energy today and tomorrow.* Proceedings of the IEEE, 2001. **89**(8): p. 1216-1226.
3. Resources, D.o.M. and Energy, *Integrated Resource Plan 2019*. 2019, Republic of South Africa, Department of Energy Pretoria, South Africa.
4. Anees, A.S. *Grid integration of renewable energy sources: Challenges, issues and possible solutions*. in *2012 IEEE 5th India International Conference on Power Electronics (IICPE)*. 2012. IEEE.
5. Buraimoh, E., et al. *South Africa Electricity Supply System: The Past, Present and The Future*. in *2020 IEEE PES/IAS PowerAfrica*. 2020. IEEE.
6. Qiao, W. and R.G. Harley. *Grid connection requirements and solutions for DFIG wind turbines*. in *2008 IEEE Energy 2030 Conference*. 2008. IEEE.
7. Castellani, F., et al. *Wind power forecasting techniques in complex terrain: ANN vs. ANN-CFD hybrid approach*. in *Journal of Physics: Conference Series*. 2016. IOP Publishing.
8. Secretariat, R., *Grid connection code for renewable power plants (RPPs) connected to the electricity transmission system (TS) or the distribution system (DS) in South Africa.* Eskom Transmission Division, PO Box, 2012. **103**.
9. Nobela, O.N., R.C. Bansal, and J.J. Justo, *A review of power quality compatibility of wind energy conversion systems with the South African utility grid.* Renewable Energy Focus, 2019. **31**: p. 63-72.
10. Ntuli, W.K., G. Sharma, and M. Kabeya. *Study of Fault Ride-Through Capability of Doubly Fed Induction Generator Based Wind Turbine*. in *2022 30th Southern African Universities Power Engineering Conference (SAUPEC)*. 2022. IEEE.
11. Nhlapo, B. and K. Awodele. *Review and comparison of the South African grid code requirements for wind generation with the European countries' grid codes*. in *2020 International SAUPEC/RobMech/PRASA Conference*. 2020. IEEE.
12. Villena-Ruiz, R., et al., *Requirements for Validation of Dynamic Wind Turbine Models: An International Grid Code Review.* Electronics, 2020. **9**(10): p. 1707.
13. Pao, L.Y. and K.E. Johnson. *A tutorial on the dynamics and control of wind turbines and wind farms*. in *2009 American Control Conference*. 2009. IEEE.
14. Wu, B., et al., *Power conversion and control of wind energy systems*. 2011: John Wiley & Sons.
15. Çetin, N., et al., *Assessment of optimum tip speed ratio of wind turbines.* Mathematical and Computational Applications, 2005. **10**(1): p. 147-154.
16. Wu, B., et al., *Power conversion and control of wind energy systems*. Vol. 76. 2011: John Wiley & Sons.
17. Abdullah, M.A., et al., *A review of maximum power point tracking algorithms for wind energy systems.* Renewable and sustainable energy reviews, 2012. **16**(5): p. 3220-3227.
18. Yap, K.Y., C.R. Sarimuthu, and J.M.-Y. Lim, *Artificial intelligence based MPPT techniques for solar power system: A review.* Journal of Modern Power Systems and Clean Energy, 2020. **8**(6): p. 1043-1059.
19. Kim, D.-C., et al., *Modeling and MPPT control in DFIG-based variable-speed wind energy conversion systems by using RTDS.* Journal of International Council on Electrical Engineering, 2011. **1**(4): p. 430-436.
20. Thongam, J.S. and M. Ouhrouche, *MPPT control methods in wind energy conversion systems.* Fundamental and advanced topics in wind power, 2011. **15**: p. 339-360.

21. Kadri, A., H. Marzougui, and F. Bacha. *MPPT control methods in wind energy conversion system using DFIG*. in *2016 4th International Conference on Control Engineering & Information Technology (CEIT)*. 2016. IEEE.
22. Cheng, M. and Y. Zhu, *The state of the art of wind energy conversion systems and technologies: A review.* Energy conversion and management, 2014. **88**: p. 332-347.
23. Yang, B., R. Liu, and X. Chen, *Sparse time-frequency representation for incipient fault diagnosis of wind turbine drive train.* IEEE Transactions on Instrumentation and Measurement, 2018. **67**(11): p. 2616-2627.
24. Boukhezzar, B. and H. Siguerdidjane, *Nonlinear control of a variable-speed wind turbine using a two-mass model.* IEEE transactions on energy conversion, 2010. **26**(1): p. 149-162.
25. Xu, Z. and Z. Pan. *Influence of different flexible drive train models on the transient responses of DFIG wind turbine*. in *2011 International Conference on Electrical Machines and Systems*. 2011. IEEE.
26. Singh, V.P., et al., *Small-signal stability analysis for two-mass and three-mass shaft model of wind turbine integrated to thermal power system.* Computers & Electrical Engineering, 2019. **78**: p. 271-287.
27. Muyeen, S., et al., *Comparative study on transient stability analysis of wind turbine generator system using different drive train models.* IET Renewable Power Generation, 2007. **1**(2): p. 131-141.
28. Murthy, S., et al. *A comparative study of fixed speed and variable speed wind energy conversion systems feeding the grid*. in *2007 7th International Conference on Power Electronics and Drive Systems*. 2007. IEEE.
29. Olivares, D.E., et al., *Trends in microgrid control.* IEEE Transactions on smart grid, 2014. **5**(4): p. 1905-1919.
30. Hu, J., et al., *Modeling of grid-connected DFIG-based wind turbines for DC-link voltage stability analysis.* IEEE Transactions on Sustainable Energy, 2015. **6**(4): p. 1325-1336.
31. Wen, B., et al., *Impedance-based analysis of grid-synchronization stability for three-phase paralleled converters.* IEEE Transactions on Power Electronics, 2015. **31**(1): p. 26-38.
32. Addoweesh, K.E. and A.L. Mohamadein, *Microprocessor based harmonic elimination in chopper type AC voltage regulators.* IEEE transactions on power electronics, 1990. **5**(2): p. 191-200.
33. Nguyen, P.-L., et al. *Synchronverter-based operation of STATCOM to mimic synchronous condensers*. in *2012 7th IEEE conference on industrial electronics and applications (ICIEA)*. 2012. IEEE.
34. Lopes, J.P., C.L. Moreira, and A. Madureira, *Defining control strategies for microgrids islanded operation.* IEEE Transactions on power systems, 2006. **21**(2): p. 916-924.
35. Gui, Y., et al., *Control of grid-connected voltage-source converters: The relationship between direct-power control and vector-current control.* IEEE Industrial Electronics Magazine, 2019. **13**(2): p. 31-40.
36. Bhutto, D.K., et al. *Wind energy conversion systems (WECS) generators: A review*. in *2019 2nd International Conference on Computing, Mathematics and Engineering Technologies (iCoMET)*. 2019. IEEE.
37. Flynn, M.P. and D.J. Allstot, *CMOS folding A/D converters with current-mode interpolation.* IEEE Journal of Solid-State Circuits, 1996. **31**(9): p. 1248-1257.
38. Wang, H., et al., *DC-link current optimal control of current source converter in DFIG.* CPSS Transactions on Power Electronics and Applications, 2021. **6**(2): p. 127-135.
39. Gnanasambandam, K., et al. *A Novel Optimal Space Vector Modulation Technique of Current Source Inverter for Solar Power Integration*. in *2018 IEEE International Conference on Power Electronics, Drives and Energy Systems (PEDES)*. 2018. IEEE.

40. Li, P., J. Wang, and J. Bai. *A Passivity-Based Control Strategy for Three-Phase Current Source Inverter Based on Interconnection and Damping Assignment*. in *2018 10th International Conference on Modelling, Identification and Control (ICMIC)*. 2018. IEEE.
41. Umoh, K. and M. Lemon, *Drivers for and barriers to the take up of floating offshore wind technology: a comparison of Scotland and South Africa.* Energies, 2020. **13**(21): p. 5618.
42. Tanvir, A.A., A. Merabet, and R. Beguenane, *Real-time control of active and reactive power for doubly fed induction generator (DFIG)-based wind energy conversion system.* Energies, 2015. **8**(9): p. 10389-10408.
43. Sujod, M.Z., I. Erlich, and S. Engelhardt, *Improving the reactive power capability of the DFIG-based wind turbine during operation around the synchronous speed.* IEEE Transactions on Energy Conversion, 2013. **28**(3): p. 736-745.
44. Jamal, A., S. Suripto, and R. Syahputra, *Performance evaluation of wind turbine with doubly-fed induction generator.* International Journal of Applied Engineering Research (IJAER), 2016. **11**(7): p. 4999-5004.
45. Banerjee, S., D. Joshi, and M. Singh, *Genetic algorithm approach for efficiency maximization and power factor enhancement of a grid connected doubly fed induction generator.* Journal of Information and Optimization Sciences, 2019. **40**(2): p. 535-545.
46. Erlich, I., M. Wilch, and C. Feltes. *Reactive power generation by DFIG based wind farms with AC grid connection*. in *2007 European Conference on Power Electronics and Applications*. 2007. IEEE.
47. Hamane, B., et al. *Direct active and reactive power control of DFIG based WECS using PI and sliding mode controllers*. in *IECON 2014-40th Annual Conference of the IEEE Industrial Electronics Society*. 2014. IEEE.
48. Kaloi, G.S., J. Wang, and M.H. Baloch, *Active and reactive power control of the doubly fed induction generator based on wind energy conversion system.* Energy Reports, 2016. **2**: p. 194-200.
49. Singh, S.K., et al., *A survey and study of different types of PWM techniques used in induction motor drive.* International journal of engineering science & advanced technology, 2014. **4**(1): p. 18-22.
50. Holmes, D.G. and T.A. Lipo, *Pulse width modulation for power converters: principles and practice*. Vol. 18. 2003: John Wiley & Sons.
51. Benbouhenni, H., *A comparison study between fuzzy PWM and SVM inverter in NSMC control of stator active and reactive power control of a DFIG based wind turbine systems.* International Journal of Applied Power Engineering (IJAPE), 2019. **8**(1): p. 78-92.
52. Kayikci, M. and J.V. Milanovic, *Reactive power control strategies for DFIG-based plants.* IEEE transactions on energy conversion, 2007. **22**(2): p. 389-396.
53. Xu, L. and P. Cartwright, *Direct active and reactive power control of DFIG for wind energy generation.* IEEE Transactions on energy conversion, 2006. **21**(3): p. 750-758.
54. Raju, S.K. and G. Pillai, *Design and implementation of type-2 fuzzy logic controller for DFIG-based wind energy systems in distribution networks.* IEEE Transactions on Sustainable Energy, 2015. **7**(1): p. 345-353.
55. Castillo, O. and P. Melin, *A review on interval type-2 fuzzy logic applications in intelligent control.* Information Sciences, 2014. **279**: p. 615-631.
56. Dida, A., F. Merahi, and S. Mekhilef, *New grid synchronization and power control scheme of doubly-fed induction generator based wind turbine system using fuzzy logic control.* Computers & Electrical Engineering, 2020. **84**: p. 106647.
57. Ismail, M.M. and A.F. Bendary, *Protection of DFIG wind turbine using fuzzy logic control.* Alexandria Engineering Journal, 2016. **55**(2): p. 941-949.
58. Dida, A. and D. Benattous, *A complete modeling and simulation of DFIG based wind turbine system using fuzzy logic control.* Frontiers in Energy, 2016. **10**(2): p. 143-154.

59. Bharti, O.P., R. Saket, and S. Nagar, *Controller design of DFIG based wind turbine by using evolutionary soft computational techniques.* Engineering, Technology & Applied Science Research, 2017. **7**(3): p. 1732-1736.
60. Yang, B., et al., *Grouped grey wolf optimizer for maximum power point tracking of doubly-fed induction generator based wind turbine.* Energy conversion and management, 2017. **133**: p. 427-443.
61. Lin, W.-M., C.-M. Hong, and C.-H. Chen, *Neural-network-based MPPT control of a stand-alone hybrid power generation system.* IEEE transactions on power electronics, 2011. **26**(12): p. 3571-3581.
62. Suryoatmojo, H., et al. *Optimal controller for doubly fed induction generator (DFIG) using Differential Evolutionary Algorithm (DE)*. in *2015 International Seminar on Intelligent Technology and Its Applications (ISITIA)*. 2015. IEEE.
63. Alhato, M.M. and S. Bouallègue, *Direct power control optimization for doubly fed induction generator based wind turbine systems.* Mathematical and Computational Applications, 2019. **24**(3): p. 77.
64. Castillo, O., et al., *A comparative study of type-1 fuzzy logic systems, interval type-2 fuzzy logic systems and generalized type-2 fuzzy logic systems in control problems.* Information Sciences, 2016. **354**: p. 257-274.
65. Raju, S.K. and G.N. Pillai, *Design and implementation of type-2 fuzzy logic controller for DFIG-based wind energy systems in distribution networks.* IEEE Transactions on Sustainable Energy, 2015. **7**(1): p. 345-353.
66. Pretorius, W.W., *Ecology and calling behaviour of the anurans of northern Zululand, South Africa*. 2019, North-West University (South Africa). Potchefstroom Campus.
67. Abad, G. and G. Iwanski, *Properties and control of a doubly fed induction machine.* Power electronics for renewable energy systems, transportation and industrial applications, 2014. **18**: p. 270-318.
68. Singhala, P., D. Shah, and B. Patel, *Temperature control using fuzzy logic.* arXiv preprint arXiv:1402.3654, 2014.